CONCENTRATED SOLAR DRIVEN *IN-SITU* RESOURCE UTILIZATION FOR LUNAR EXPLORATION

A Thesis
Presented to
The Academic Faculty

by

Ashley R. Clendenen

In Partial Fulfillment
of the Requirements for the Degree
Master of Science in Mechanical Engineering

Georgia Institute of Technology

August 2020

CONCENTRATED SOLAR DRIVEN *IN-SITU* RESOURCE UTILIZATION FOR LUNAR EXPLORATION

Approved by:

Dr. Peter Loutzenhiser, Advisor
George W. Woodruff School of
Mechanical Engineering
Georgia Institute of Technology

Dr. Thomas Orlando, Advisor
School of Chemistry and Biochemistry
Georgia Institute of Technology

Dr. Zhuomin Zhang
George W. Woodruff School of
Mechanical Engineering
Georgia Institute of Technology

Dr. Brant Jones
School of Chemistry and Biochemistry
Georgia Institute of Technology

Date Approved: July 20, 2020

For my family

For Dr. William Greenwood - without whose encouragement I would not have applied to Georgia Tech

And for Lia - hands down the best Clendewinskie

ACKNOWLEDGEMENTS

I would like to thank my advisors, Dr. Loutzenhiser and Dr. Orlando, for their guidance on my research. I would also like to thank my committee members, Dr. Brant Jones and Dr. Zhuomin Zhang, for their input on my thesis. Further, I would like to thank Dr. Alexandr Aleksandrov for assisting with the TPD experiments.

Thank you to my colleuges in the Solar Fuels and Technology Lab, Malavika Bagepalli, Evan Bush, Tyler Farr, Ty Nguyen, Garrett Schieber, Andrew Schrader, and Justin Yarrington, for creating an ejoyable, friendly evironment in which to do research and for their helpful suggestions on my research. I enjoyed our lab lunches and conversations.

Finally, I would like to thank my family, Papa, Grandma Pam, Dad, Jonathan, Austin, Amanda, Anthony, and Aaron, for the countless hours of encouragement and never ceasing to brighten even the most stressful days. Esspessially, I would like to thank my Mum for giving me advice, proof reading papers she didn't understand, and listening to me practice my presentations over and over and over. Without my family, I certainly wouldn't have been able to do this.

This work was carried out as part of REVEALS which was directly supported by the NASA Solar System Exploration Research Virtual Institute cooperative, agreement number NNA17BF68A.

TABLE OF CONTENTS

LIST OF TABLES

LIST OF FIGURES

LIST OF SYMBOLS AND ABBREVIATIONS

Symbols

A	aperture area of a solar reactor, projected area of the particle
A_{eff}	effective surface area
C	circularity
$\tilde{C}$	solar concentration ratio
d_{eff}	effective diameter
Δm_{loss}	change in mass
E	total solar energy impinging upon the lunar surface
ΔE_{des}	energy of desorption
G	Gibb's free energy
$\overline{G}_{\text{D}}$	average direct solar irradiation
G_{DN}	direct-normal irradiation
G_{ext}	extraterrestrial solar irradiance
H	height
$H_{\text{products,T}}$	enthalpy of a product at a specific temperature
$H_{\text{reactans, T}_{\text{i}}}$	enthalpy of a reactant at the initial conditions
$\Delta H_{\text{reaction}}$	reaction enthalpy
m_{H_2}	mass of hydrogen
$m_{\text{H}_2\text{O}}$	mass of water
m_{i}	initial mass
m_{O}	mass of O

m_{O_2}	mass of O_2
m_{Regolith}	mass regolith
$m_{\text{Volatiles}}$	mass of volatile
N	Day of the Year
n	order of desorption
n_{bin}	bin count
P	perimeter of the particle
q''_{solar}	spatial solar radiative heat flux
Q_{net}	net solar energy absorbed by a solar reactor
Q_{solar}	incoming solar energy
R	radius between the sun and the Earth/Moon system, ideal gas constant, roundness
t	time
T	time dependent temperature, temperature
T^{eq}	equilibrium temperature
T_{reactor}	operating temperature of a reactor
$\eta_{\text{absorption}}$	theoretical absorption efficiency
θ	time dependent adsorbate coverage
θ_z	zenith angle on the lunar surface
$d\theta / dt$	rate of desorption
2θ	diffraction angle
ν	frequency factor
σ	Stefan-Boltzmann constant
Ω_{sun}	solid angle of the sun

Acronyms

BET	Brunauer–Emmett–Teller
CEIL	Ceiling Limit
CLASS	Center for Lunar & Asteroid Surface Science
DSC	Differential Scanning Calorimetry
GC	Gas Chromatography
HL	Highland
HTM	High-Titanium Mare
ISRU	*In-Situ* Resources Utilization
JSC-1A	Johnson Space Center - 1A (regolith simulant)
LAMP	Lyman-Alpha Mapping Project
LCROSS	Lunar Crater Observation and Sensing Satellite
LHS-1	Lunar Highlands Simulant - 1 (regolith simulant)
LMS-1	Lunar Mare Simulant - 1 (regolith simulant)
LRO	Lunar Reconaissance Orbiter
LTM	Low-Titanium Mare
MS	Mass Spectrometry
NP	North Pole
QMS	Quadrupole Mass Spectrometer
SP	South Pole
STEL	Short Term Exposure Limit
TGA	Thermogravimetric Analysis
TLV	Threshold Limit Values

TPD	Temperature Programmed Desorption
TWA	Time Weighted Average
UHP	Ultra High Purity
UHV	Ultra-High Vacuum
XRD	X-Ray Diffractometry

SUMMARY

This work seeks to develop a theoretical framework for using concentrated solar irradiation to drive *in-situ* resource utilization processes, which are required for fiscally feasible lunar missions. The thermal extraction of volatiles, primarily H_2O, and thermochemical processing of lunar regolith to extract O_2 are explored in this work.

Models are presented explore equilibrium compositions as a function of temperature at lunar pressure, specifically for O_2, H_2O, and metals and metalloids. Predictions for potentially harmful toxins are also presented, due to the presence of volatiles other than water in lunar permanently shadowed regions, in order to examine if dangerous amounts of toxins will be released during extraction of H_2O from the lunar regolith. A simplified model of the solar resources available on the Moon is also presented, which, though simplified, can provide insight into where *in-situ* resource utilization facilities should be placed to utilize the solar resources most effectively. Both these models are used to suggest specific concentrating infrastructure for use for specific.

The results of some preliminary proof-of concept experiments are also presented. Thermodynamic analysis experiments with lunar regolith simulants suggests that the thermal extraction of H_2O is, in fact, possible. Composition and structure of regolith simulants before and after thermodynamic analysis, as determined by x-ray diffraction, are presented. The desorption energies of lunar regolith simulants is presented, determined by leading edge analysis of temperature programmed desorption.

CHAPTER 1. INTRODUCTION

1.1 Motivation

Humanity is moving to go "Forward to the Moon." Eventually establishing a permanent human base on the lunar surface [1] and using it as a launch point for missions to Mars [2], requires that many exploration related problems be solved. The establishment of a base on the Moon is fraught with challenges and perils to human survival at the most basic level. The lunar environment is harsh and devoid of the most rudimentary elements that are required for habitation, including readily accessible water and oxygen. In the absences of an atmosphere and a strong magnetic field, equipment and personnel are also subjected to deadly radiation (including galactic cosmic rays and dangerous particles produced in solar particle events) that threatens long-term survival by increasing the probability of developing cancers or other major health problems [3]. In order to sustain habitation on the surface of the Moon, lunar resources must be utilized to address these challenges. Research in the area of *in-situ* resource utilization (ISRU) has focused on addressing these challenges with an underlying goal of exploiting the natural lunar resources. This will minimize the transportation of materials from the Earth and thus reduce the number of expensive launches.

One of the most important resources for human habitation and rocket propellant is oxygen. A potential source for oxygen on the Moon is the regolith itself, which contains a considerable amount of bound oxygen by weight [4]. Extracting this oxygen provides an on-demand, and virtually inexhaustive, supply of propellant and breathable air.

An equally important resource is water, which is required for drinking or splitting into hydrogen and oxygen via electrolysis [5]. Hydrogen is present on the Moon in two main forms, which will be discussed later. This hydrogen could be used to provide water for a crewed lunar mission. However, there are two major problems with using the lunar hydrogen supply as the only water source for a crew. The first is the amount of regolith that would have to be processed to extract enough water to sustain life, and the second is the presence of volatiles, other than water, in the regolith [6-8].

Regardless of the ISRU technique that is being considered, some sort of power or heat source must be developed to drive the process. The Moon is ideally situated to exploit solar irradiation as a high-temperature heat source to drive thermochemical reactions or thermal processes for ISRU applications.

1.2 Objectives

The focus of this work is to develop a theoretical framework for using concentrated solar irradiation to drive the thermal extraction of volatiles, primarily water, and thermochemical processing of lunar regolith to extract oxygen, lower valence metal oxides, metals, and metalloids. The theoretical limitations and optimal conditions for concentrating solar irradiation are examined for different regions of the Moon. This, paired with a knowledge of the chemical composition of the lunar regolith in each region, will be essential in determining the ideal locations for setting up ISRU facilities to collect specific resources. Additionally, the release of potentially harmful volatiles is examined to determine if dangerous amounts of these volatiles are freed during extraction of water from the ice mix with the lunar regolith.

These analyses are performed by examining predicted chemical equilibrium compositions as functions of pressure and temperature for different regolith compositions. Different thermal and thermochemical processes are then matched to different solar concentrating infrastructure. These theoretical predictions are tested by some initial experiments.

1.3 Thesis Overview

To fully study the extraction of water and oxygen from lunar regolith, a few things must be considered. Among these are the solar resources, the composition of the regolith, and the other volatiles present in the regolith. To create a groundwork for lunar driven thermal extraction of water and thermochemical extraction of oxygen, this thesis includes modeling and some preliminary experiments that explore these concepts.

CHAPTER 2 is a literature review. This provides an overview of previous work done in this field upon which this work is built. This chapter also has an introduction to concentrating solar irradiation and a description on why the Moon is better situated for utilizing these solar resources than the Earth.

A preliminary map of the lunar solar resources was created to show where the best sites for utilizing solar irradiation are located. Information about this modeling is found in CHAPTER 3. The results are discussed in CHAPTER 4.

Chemical equilibrium modeling was performed to predict what would be released from the regolith at different temperatures. These predictions were made for oxygen, water, metal oxides, metals, and metalloids, as well as potentially dangerous toxins also present in the regolith and ice. Information about this modeling is found in CHAPTER 3. The results are discussed in CHAPTER 4.

To test these models, preliminary proof-of-concept, non-equilibrium experiments were performed. Thermogravimetric analysis (TGA) experiments were conducted, with mass spectrometry (MS) and gas chromatography (GC) hooked up to the TGA exhaust, to determine the total mass change and how much oxygen is released upon heating regolith simulants. Temperature programmed desorption (TPD) experiments were performed to explore the water released upon heating regolith simulants. Since particle size is important for TPD, the particle size of the regolith simulants was calculated. Information about the experimental setup is found in CHAPTER 3. The results are reported in CHAPTER 4.

CHAPTER 5 has conclusions. It also has information about future work that will support this research.

CHAPTER 2. LITERATURE REVIEW

2.1 Oxygen Extraction Techniques

O and O_2 can be used for life support or for rocket propellant [9]. Since the lunar regolith contains a large amount of bound O by weight [4], it is feasible to produce these resources *in-situ*. However, metal and metalloid oxides typically form very high strength bonds, and relatively large amounts of energy are required to break these bonds in order to extract the O_2 [10]. Some of the proposed methods of O_2 extraction are carbothermal reduction [4, 11], H_2 reduction [12-17], high-temperature thermal-electrochemical techniques (*e.g.*, electrolysis, which also produces metals) [18-20], and direct high-temperature thermal reduction (also known as pyrolysis) [21-23]. Some TGA experiments have been performed to study the reduction of lunar regolith simulant by hydrogen and methane [24].

2.2 Water Extraction Techniques

H_2O is another resource essential to sustain life. Hydrogen is present on the Moon in the form of both H_2O(s) trapped beneath the surface, especially in permanently shadowed regions near the poles [25-28], and in trace amounts as solar wind-implanted OH [29-34]. H_2O(s) was mainly deposited by carbonaceous asteroids, volcanic outgassing, and solar wind with micrometeoroid impacts [35]. The OH comes from a monolayer of H_2O molecules stably bound to the surface of the Moon with dissociative chemisorption as an hydroxyl and an hydrogen atom under ultra-high vacuum (UHV) conditions [29].

A proposed method to extract $H_2O(s)$ thermally shown in Figure 2.1. This process involves the direct surface heating of lunar regolith to volatilize the $H_2O(s)$, driving it to a collection apparatus, like a tent [36], to capture the $H_2O(v)$ [37-39]. To extract bound OH, heating the regolith is required. Recombinative desorption results in the formation of H_2O [29]. However, H_2O is not the only volatile presence in the permanently shadowed regions.

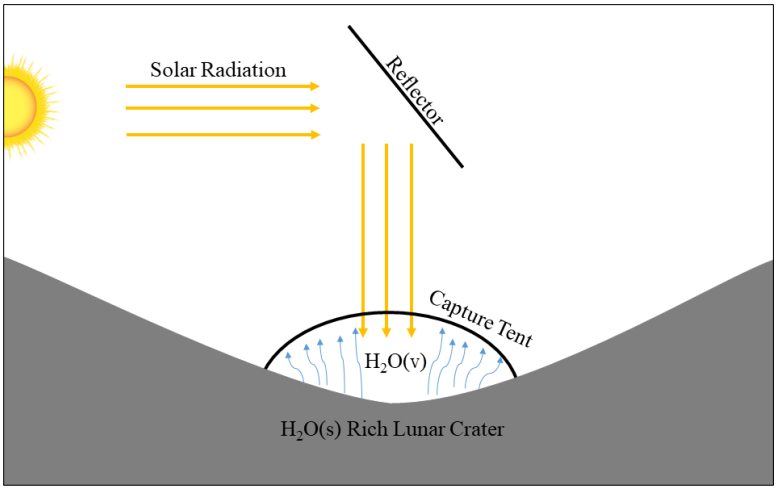

Figure 2.1. Schematic of the thermal extraction of volatiles, which uses solar irradiation reflected into an area of high $H_2O(s)$ concentration (in this case, a permanently shadowed crater) causing the $H_2O(s)$ to volatilize and be collected in a transparent capture tent.

In 2009, the Lunar Crater Observation and Sensing Satellite (LCROSS) mission used a Centaur rocket to impact a permanently shadowed region on the lunar South Pole. The resulting ejecta was observed and analyzed by a shepherding spacecraft. Many volatiles were discovered, including potentially toxic ones [6-8], as predicted over 2 decades ago before these measurements were possible [40]. Any attempt to remove $H_2O(s)$ from the lunar regolith using thermal extraction must also consider that potentially hazardous volatiles may be released simultaneously.

Another ISRU technique proposed to provide H_2O for a crewed mission is hydrogen reduction of the ilmenite in the lunar regolith [41, 42]. While there is a nearly endless

supply of ilmenite, providing enough hydrogen is problematic. In order to have enough hydrogen, it must be launched from Earth. The astronauts would consume the H_2O making the hydrogen unable to be reused and requiring continuous resupply missions.

2.3 Other ISRU Processes

On top of O_2 and H_2O extraction, extensive ISRU research has focused on using lunar regolith, coupled with additive manufacturing techniques, to provide a unique path toward permanent habitation [43]. Lunar regolith can be used as a material to fabricate bricks, concrete, or cement, either with or without non lunar based additives, which can be used for construction purposes [44-54]. These concrete blocks are joined together to create a solid structure [55]. The regolith can also be used for radiation shielding of lunar bases [56, 57]. Extensive research has also examined sintering [58-60], especially microwave sintering/melting [61-63] and selective laser melting [64-66], of the lunar regolith to create precise objects, like tools. Many other ISRU techniques exploiting regolith have also been proposed [67-73]. Many of these techniques require the lunar regolith be heated, which may lead to the release of O_2 and other volatiles. In theory, a system could be designed to catch and isolate these volatiles as they are released rather than letting them escape into space.

2.4 Solar Driven ISRU

It is estimated that a fully functional lunar base with ISRU facilities would require 1 MW_e of power during the astronaut's waking hours and 10 kW_e of power during the astronaut's night [74]. Different studies have investigated using a range of energy sources, including batteries, nuclear reactors [75], and fuel based generators to drive ISRU

processes [76]. However, all of these power sources must be transported to the Moon from the Earth. High-temperature solar irradiation is an ideal and virtually unlimited resource to provide process heat to drive ISRU processes.

There are numerous advantages to using solar irradiation to drive ISRU processes on the Moon compared to on the Earth: The Moon has no atmosphere, therefore, solar irradiation is not attenuated; there is no wind and less gravity, allowing for lighter infrastructure; the lunar tilt from the celestial equator (lunar declination angle) is only 1.5° [77], compared to the Earth's 23°, resulting in little seasonal variation in the solar irradiation; and the lunar day is equivalent to ~14 Earth days with some regions that are permanently irradiated.

There are two main limitations to utilizing the solar resources on the Moon. The primary limitation is that the solar irradiation is relatively dilute. However, this is overcome by concentrating solar irradiation to provide the necessary radiative heat fluxes to drive the volatilization of H_2O and/or the thermochemical processes to extract O_2 from lunar regolith. The other limitation is storage of energy for use during the lunar night. Some research has investigated using the regolith itself as a thermal energy storage medium, though as of yet this method is not viable enough to rival storage methods that must be launched from Earth, even considering the launch cost [78].

2.4.1 Concentrating Technologies

Highly concentrated solar irradiation has been used for process heat for electricity production [79] or for driving thermochemical processes [79]. The metric for comparing solar concentration infrastructure is the average solar concentration ratio, $\tilde{C}$, (with units of

"suns," where 1 sun is equal to 1000 W/m^2, the direct-normal solar irradiation at the surface of the Earth) defined accounting for optical and projection losses as:

$$\tilde{C} = \frac{\frac{1}{A}\int_A q''_{\text{solar}} dA}{G_{\text{DN}}} \tag{1}$$

where q''_{solar} is the spatial solar radiative heat flux, G_{DN} is the direct-normal solar irradiation, and A is the aperture area of a solar reactor. q''_{solar} is a strong function of solid angle of the sun, Ω_{sun}, which is inversely proportional to radius between the sun and the Earth/Moon system squared, R^2; therefore, larger Ω_{sun} result in smaller $\tilde{C}$ for the same solar concentrating infrastructure [80].

Three main types of solar concentrating technologies are shown in Figure 2.2. Trough systems [Figure 2.2 (a)] are capable of $30 \leq \tilde{C} \leq 100$ suns using a one-axis tracking system to direct incoming solar rays to a linear receiver. Tower systems [Figure 2.2 (b)] are capable of $500 \leq \tilde{C} \leq 5000$ suns using heliostats with two-axis tracking to direct the sun's rays to receivers mounted on a tower. Lower $\tilde{C}$ are possible by reducing the number of heliostats in the field. Parabolic dishes [Figure 2.2 (c)] are capable of $1000 \leq \tilde{C} \leq 10{,}000$ suns using two-axis tracking to direct the sun's rays to a receiver mounted in the focus [81]. Using similar technologies on the surface of the Moon affords a unique opportunity to harness the sun for ISRU thermochemical processes.

These technologies utilize mirrors to concentrate the solar irradiation. Research has been done to fabricate mirrors with ISRU methods, using glass produced from lunar

regolith with a reflective surface of aluminum on one side of the glass. These mirrors were found to have an average reflectivity as high as 80% over wavelengths between 400 nm and 1250 nm [82].

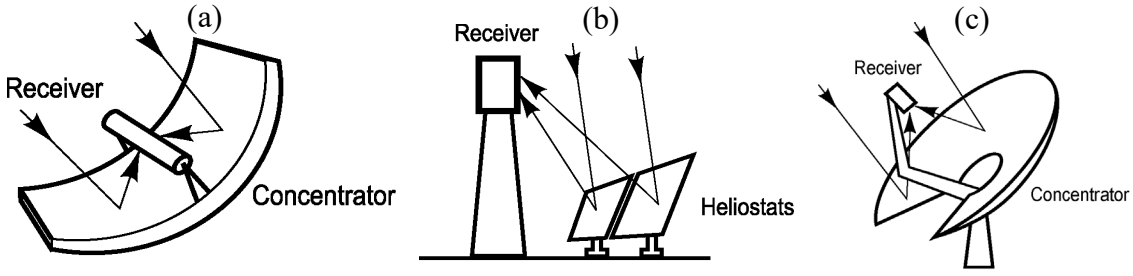

Figure 2.2. Schematic depictions of solar concentrating infrastructures that are currently used for electricity generation and solar thermochemistry applications: a) a trough system; b) a power tower system with heliostats; and c) a paraboloidal dish system. (Image from [81]; used with permission).

ISRU thermochemical processes for a range of different temperatures must be matched to different solar concentrating infrastructures. A theoretical solar receiver/reactor is assumed for evaluation purposes to be a blackbody, a cavity receiver that is perfectly insulated with an emissivity and absorptivity approaching unity. The theoretical metric for performance is the absorption efficiency, given by:

$$\eta_{\text{absorption}} = \frac{Q_{\text{net}}}{Q_{\text{solar}}} = 1 - \frac{\sigma T_{\text{reactor}}^4}{G_{\text{DN}} \tilde{C}} \tag{2}$$

where Q_{net} is the net solar energy absorbed by the solar reactor; Q_{solar} is the incoming solar energy; σ is the Stefan-Boltzmann constant; and T_{reactor} is the operating temperature of the reactor. $\eta_{\text{absorption}}$ is the theoretical maximum for a solar cavity reactor. Decreases for actual infrastructure are associated with different reactor designs. Windowed solar reactors have transmission losses [83], while indirect heating of an absorber plate/tube results in losses

associated with heat conduction. $\eta_{absorption}$ will be unaffected by changes in G_{DN} that result from changes in R as G_{DN} is proportional to R^2, Ω_{sun} is inversely proportional to R^2, hence, $\tilde{C}$ for the same solar concentrating infrastructure increase at the same rate as G_{DN} decreases, result in the product $G_{DN}\tilde{C}$ remaining constant for different R's. However, differences in G_{DN} on the Earth compared to the Moon result from attenuation.

The $\eta_{absorption}$ as a function of $T_{reactor}$ is provided for a range of $50 < \tilde{C} < 10{,}000$ suns in Figure 2.3 to compare $\eta_{absorption}$ for the Moon (G_{DN} = 1365 W/m^2) to Earth (G_{DN} = 1000 W/m^2) for R = 1.0 AU. Higher $\eta_{absorption}$ occur on the Moon than on Earth at all but the lower $T_{reactor}$ due to a higher G_{DN} in the absence of attenuation. The $\eta_{absorption}$ was near unity at lower $T_{reactor}$ due to re-radiative losses to the surroundings. The $\eta_{absorption}$ rapidly decreased at higher $T_{reactor}$'s as the re-radiation losses (proportional to $T_{reactor}^4$) increase. The maximum $T_{reactor}$, or the stagnation temperature, corresponded to the point where all of the absorbed irradiation is re-emitted to the surroundings, resulting in $\eta_{absorption}$ of 0. The stagnation temperature increased with higher $\tilde{C}$'s.

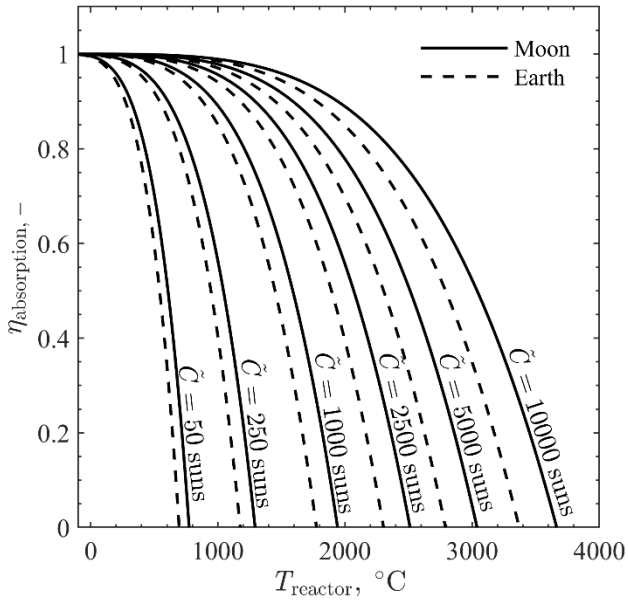

Figure 2.3. Theoretical absorption efficiency on the Moon (solid lines) and Earth (dashed lines) as a function of solar reactor temperature for a range of solar concentration ratios between 50 and 10,000 suns.

These results can be linked to different concentrating infrastructures for different thermal/thermochemical processes. For lower temperature processes, solar trough technology is ideal, for example T_{reactor} = 610 °C at $\tilde{C}$=50 suns for $\eta_{\text{absorption}}$ = 0.5. Higher temperature thermochemical processes require higher $\tilde{C}$'s. The power tower is ideal to drive solar thermochemical processes operating at higher temperature, for example T_{reactor} = 2070 °C at $\tilde{C}$=2500 suns for $\eta_{\text{absorption}}$ = 0.5. Both the troughs and the power towers can operate at very large scales; however, the $\tilde{C}$ fluctuates throughout the lunar day due to projection, or cosine, losses as the angles of incidence change with respect to the mirrors. The paraboloidal dishes are capable of achieving the highest $\tilde{C}$'s without projection losses, for example $\eta_{\text{absorption}}$ = 0.5 corresponds to T_{reactor} = 2510 and 3040 °C for $\tilde{C}$ = 5000 and 10,000 suns, respectively. The scale of paraboloidal dishes is smaller, and the solar reactor must be mounted in the focus during operation. However, the dishes are modular and may

be deployed in areas of ideal sun to drive relevant ISRU processes to permit human habitation.

2.4.2 Solar Driven ISRU Projects

Figure 2.4 shows a schematic of different pathways to exploit concentrated irradiation for ISRU. Regolith is mined and transported to a location for processing [84, 85]. This may include the development of construction or shielding materials or tools, either directly or through additive manufacturing techniques. This may also include H_2O and O_2 production via the chemical reduction of metal and metalloid oxides with H_2 or C, and H_2O isolation via thermal extraction. This may further include high-temperature thermochemical reaction used to produce H_2O, O_2, and valuable metals and metalloids.

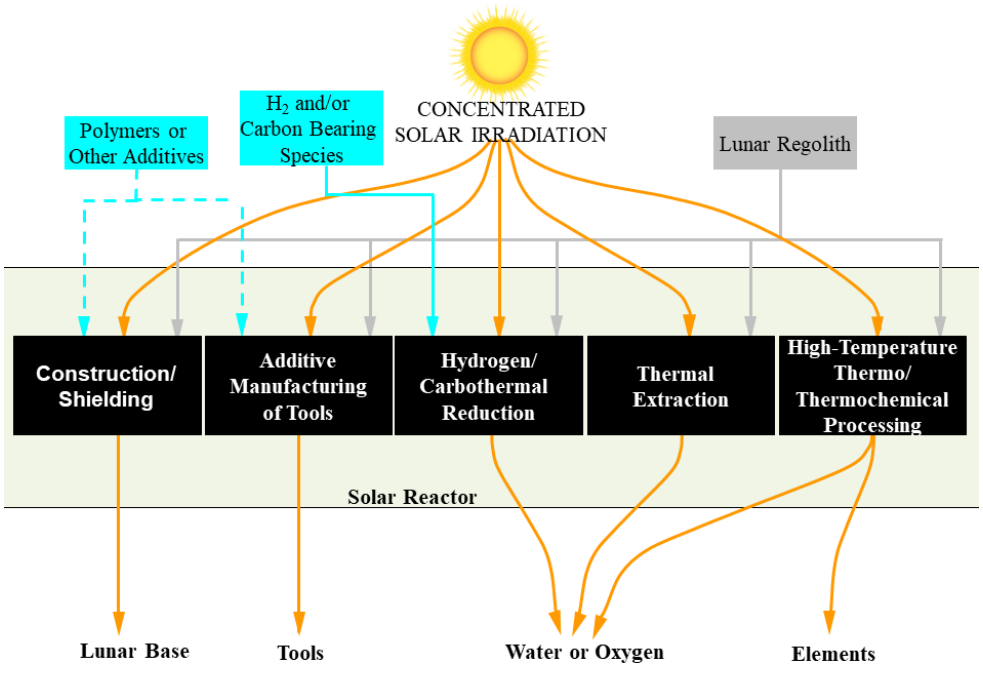

Figure 2.4. Schematic of possible solar-driven *in-situ* resource utilization processes.

Research has begun in a few of the categories listed in Figure 2.4. An optical waveguide system was designed to concentrate solar irradiation for a number of

applications, including the carbothermal reduction of lunar regolith [5, 86]. A heat pipe solar receiver utilizing concentrated solar irradiation was used for hydrogen reduction of the lunar regolith [87]. Hydrogen reduction of ilmenite using concentrated solar irradiation has also been studied in a system with the capacity to process 25 kg of material at a time [88]. Concentrated solar irradiation was also used in the direct high temperature thermochemical reduction, or pyrolysis, of lunar soil [21]. Other work focused on using concentrated solar irradiation to sinter lunar regolith without a binding agent [89, 90]. Concentrated solar irradiation was also used to sinter regolith with added polymers to stabilize the lunar surface for a launch or landing pad [91]. Concentrated solar irradiation, beamed into permanently shadowed areas, was investigated for the thermal extraction of volatiles, such as H_2O [92].

CHAPTER 3. MATERIALS, MODELING, AND METHODS

3.1 Materials

3.1.1 Chemical Composition of Lunar Regolith

Lunar regolith consists primarily of metal oxides that form complex minerals, resulting a composition that is ~45% O by weight [4]. The elemental composition of lunar regolith changes for different parts of the Moon. The three different types of lunar regolith are 1) highlands regolith (HL), 2) high-titanium mare regolith (HTM), and 3) low-titanium mare regolith (LTM) which are dispersed over the Moon. Each was examined in this work. HL is more abundant than HTM and LTM and covers 84% of the nearside of the Moon and 99% of the farside of the Moon [93]. The oxide compositions are shown in Table 3.1. HL contains the highest relative amounts of Al_2O_3 and CaO while both HTM and LTM contain larger amounts of FeO. All of the regolith contains similar amounts of both MgO and SiO_2, which account for a large part of their composition.

Table 3.1. Oxides species compositions of the highlands, high-titanium mare, and low-titanium mare lunar regolith in weight percent [94].

Oxide Species	Highlands (wt%)	High-Titanium Mare (wt%)	Low-Titanium Mare (wt%)
Al_2O_3	25.1	12.4	13.2
CaO	14.9	11.4	10.8
Cr_2O_3	0.1	0.4	0.4
FeO	6.3	16.6	17.2
K_2O	0.1	0.1	0.2
MgO	7.6	8.9	10.0
MnO	0.1	0.2	0.2
Na_2O	0.4	0.4	0.4
P_2O_5	0.1	0.1	0.2

Table 3.1. Continued. Oxides species compositions of the highlands, high-titanium mare, and low-titanium mare lunar regolith in weight percent [94].

Oxide Species	Highlands (wt%)	High-Titanium Mare (wt%)	Low-Titanium Mare (wt%)
SiO_2	45.0	41.0	45.4
TiO_2	0.5	8.5	2.9

3.1.2 Regolith Simulants

Since lunar samples are rare, regolith simulants were used for all experiments discussed in this thesis. Three different regolith simulants were used for experiments, JSC-1A, LMS-1, and LHS-1. JSC-1A was developed by NASA as a Mare simulant [95]. LMS-1 and LHS-1 were developed by the Center for Lunar & Asteroid Surface Science (CLASS) Exolith Lab at the University of Central Florida as a Mare simulant and a Highlands simulant, respectively [96, 97]. The chemical compositions of each regolith simulant are listed in Table 3.2.

Table 3.2. Oxides species compositions of the JSC-1A, LMS-1, and LHS-1 lunar regolith simulants in weight percent.

Oxide Species	JSC-1A [95] (wt%)	LMS-1 [96] (wt%)	LHS-1 [97] (wt%)
Al_2O_3	16.2	14.13	26.24
CaO	10.0	5.94	11.62
Cr_2O_3	-	0.21	0.02
FeO	-	7.87	3.04
Fe_2O_3	12.4	-	-
K_2O	0.8	0.57	0.46
MgO	8.7	18.89	11.22
MnO	0.2	0.15	0.05
Na_2O	3.2	4.92	2.30
P_2O_5	0.7	-	-

Table 3.2. Continued. Oxides species compositions of the JSC-1A, LMS-1, and LHS-1 lunar regolith simulants in weight percent.

Oxide Species	JSC-1A [95] (wt%)	LMS-1 [96] (wt%)	LHS-1 [97] (wt%)
SiO_2	45.7	42.81	44.18
TiO_2	1.9	4.62	0.79
SO_3	-	0.11	0.10

3.1.3 Hydrogen Bearing Species in the Lunar Soil

Hydrogen is present on the Moon as OH and H_2O(s). The abundance of bound OH at specific locations on the Moon is shown in Table 3.3 [98]. For the purpose of modeling, H_2 was added to account for the OH. This modeling amount is also shown in Table 3.3.

Table 3.3. Abundance of OH present in lunar regolith at difference location on the lunar surface [98] and amount of H_2 used for modeling.

Location	Abundance of OH	H_2 Used for Modeling
North Pole (NP)	1500 ppm	750 ppm
South Pole (SP)	1000 ppm	500 ppm
Equator (E)	0 ppm	0 ppm

According to measurements from the Lyman-Alpha Mapping Project (LAMP) instrument aboard the Lunar Reconaissance Orbiter (LRO), the lunar regolith in shadowed craters has ~ 0.1 to 2 wt% of H_2O(s) [99]. Modeling the H_2O(s) present in the shadowed craters predicts a slightly smaller concentration of ~0.1 to 1 wt% [35]. Additionally, these craters contain other trapped volatiles [6-8]. Some of these volatiles are potentially toxic or harmful and, therefore, must be considered for ISRU scenarios that involve permanently shadowed regions, like H_2O(s) extraction [40]. Table 3.4 shows the abundance of each volatile relative to the abundance of H_2O as measured by LCROSS at a permanently illuminated region on the South Pole [6].

Table 3.4. Abundance of each volatile relative to H_2O as measured by LCROSS [6].

Volatile	Molecular Abundance relative to H_2O
H_2O	100.00%
H_2S	16.75%
NH_3	6.03%
SO_2	3.19%
C_2H_4	3.12%
CO_2	2.17%
CH_3OH	1.5%
CH_4	0.65%
OH	0.03%

3.2 Solar Resource Modeling

Efficiently using solar irradiation as process heat to drive ISRU processes necessitates careful examination of resource allocation on the surface of the Moon. Solar concentration infrastructure must be matched with solar resources for different locations, facilitating an investigation of different ISRU scenarios based off of regolith compositions. A simplified model of the solar resources on the Moon was developed to this end.

Understanding the distribution of the solar resources on the Moon is vital to matching ISRU processes to relevant thermochemistry. The extraterrestrial solar irradiation changes throughout the year due to Earth's elliptical orbit around the sun, where the extraterrestrial solar irradiance (G_{ext}), R (radius between the sun and the Earth/Moon system, as stated above), and Ω_{sun} (solid angle of the sun, as stated above) as a function of Day of the Year (N) are given in Figure 3.1. The maximum G_{ext} of 1415 W/m^2 and minimum G_{ext} of 1321 W/m^2 correspond to N of 1 and 365, and N of 185, respectively, with an average G_{ext} of 1365 W/m^2. The maximum G_{ext} corresponds to a minimum R of 0.9829 AU and the maximum Ω_{sun} of 43.86×10^{-10} sr, while the minimum G_{ext} corresponded to a maximum R of 1.0171 AU and the minimum Ω_{sun} of 40.96×10^{-10} sr.

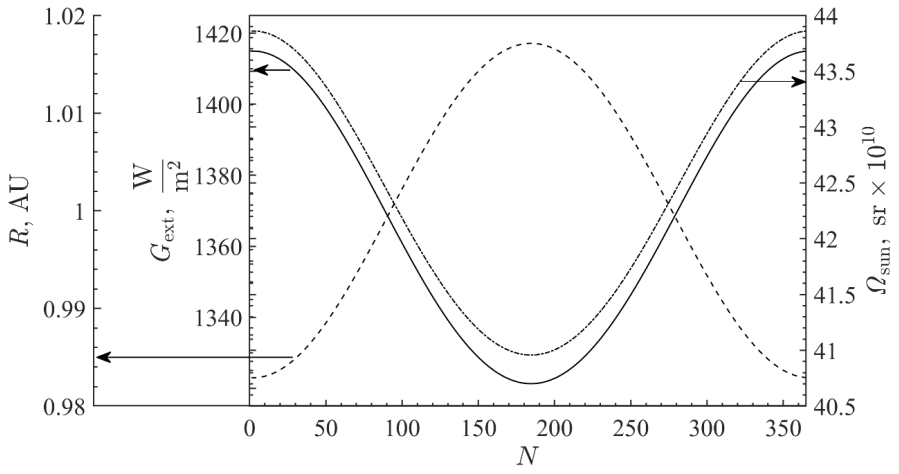

Figure 3.1. Extraterrestrial solar irradiation in W/m^2 (solid), the radius of the Earth's orbit around the sun in AU (dashed), and the solar solid angle (dashed-dotted) as a function of the day of the year (Created using the technique described in [100]).

The simplified map of the solar resource distribution, shown in the results section, neglected the declination of the Moon (1.5 °) and changes in topography with the direct-normal irradiation $G_{DN} = \overline{G}_{ext}$ =1365 W/m^2 corresponding to R of 1 AU in the absence of attenuation. The average direct solar irradiation, $\overline{G}_D$, and total solar energy impinging upon the lunar surface, E, were determined, respectively, as:

$$\overline{G}_D = \frac{G_{DN}}{t} \int_{\substack{\text{lunar} \\ \text{day}}} \cos\theta_z dt \tag{3}$$

$$E = G_{DN} \int_{\substack{\text{lunar} \\ \text{day}}} \cos\theta_z dt \tag{4}$$

where t is time; and θ_z is the zenith angle on the lunar surface.

3.3 Thermodynamic Equilibrium Modeling

Chemical equilibrium modeling was performed to forecast chemical compositions as a function of temperature and pressure for lunar regolith. Gibb's Free Energy minimization ($\Delta G = 0$) was used to predict equilibrium compositions for isobaric processes [101, 102]. The pressure on the Moon was ~ 3×10^{-15} bar [103], and the equilibrium composition of each species was normalized per unit mass of regolith. These calculations were performed for the three main types of regolith: 1) HL, 2) HTM, and 3) LTM, as well as hydrogen and toxic volatiles. Equilibrium predictions used the expected geochemical compositions but neglected the geology of the lunar regolith. Further, these results do not consider chemical kinetics, which are essential in the design of solar reactors [104].

3.4 Experimental Methods - TGA

TGA experiments were performed using a NETZSCH STA 449 F3 Jupiter simultaneous thermal analyzer with a graphite furnace which has a mass resolution of 1 μg. Crucibles created from Al_2O_3 (AdValue Technology) were used to hold the samples during experimental runs to limit any reactions between the crucible and the sample. Ultra High Purity (UHP) argon (Airgas USA, purity 5.0, ~100%) was used as a purge gas. The reported mass change was verified by weighing the sample on an analytical balance (Mettler-Toledo ML54) with resolution 0.1 mg before and after the experiments.

TGA of LMS-1 and LHS-1 were performed utilizing a sample mass of ~50 g of regolith simulant. Using a linear heating rate of 20 K/min, the sample was heated from 100°C to 1300°C. The temperature was then held constant at 1300°C for 3 hours. The change in mass was recorded every 1 s. The purge gas flow rate was of 100 mL_N/min (where mL_N is defined at 0°C and 1 atm).

TGA of JSC-1A was performed utilizing a sample mass of ~100 g of regolith simulant. For these experiments, a protective layer of platinum foil (Sigma-Aldrich 0.025 mm thick 99% Pt Foil 267244-1.4G) was placed between the sample and the Al_2O_3 crucible to further reduce the chance of a reaction. Using a linear heating rate of 20 K/min, the sample was heated from 100°C to 1500°C. The temperature was then held constant at 1500°C for 6 h. The change in mass was recorded every 1 s. The purge gas flow rate was of 200 mL_N/min.

The TGA exhaust was monitored by MS (OmniStar ThermoStar GSD320 Gas Analysis System) and GC (Agilent 490 Micro GC equipped with Molsieve and PoraPLOT Q columns). The MS sampling rate was 1 Hz. The GC was used to calibrate MS.

The experiments involving JSC-1A and LHS-1 were only conducted once, while the experiments involving LMS-1 were conducted twice. Therefore, results obtained from these experiments are preliminary. More experiments will be conducted in the future to verify these results.

3.4.1 XRD Analysis

X-ray diffractometry (XRD, PANalytical X′Pert PRO Alpha-1 diffractometer) was performed with diffraction angle, 2θ, ranging between 20–100° to examine the structure before and after the TGA runs. This was done for JSC-1A. As of yet, no XRD has been performed on LMS-1 or LHS-1.

3.5 Experimental Methods - TPD

TPD experiments were run using LMS-1 and LHS-1 samples under ultra-high vacuum (UHV) conditions, with a pressure of ~1×10^{-9} Torr. The samples were first mounted on a 25 mm thick stainless steel sample holder, and baked to remove any adsorbed gases. Then the sample was allowed to cool to the dosing temperature of 300K and exposed to the adsorbate, through a leak valve (in this case H_2O vapor). Afterward, the sample was heated by a dual-filament tungsten heater at a constant rate of 0.5 K/s. The desorption was monitored by a Quadrupole Mass Spectrometer (QMS, Pfeiffer Vacuum Prisma Plus QMG 220 C-SEM) as the sample was heated to 1000 K. The temperature was monitored by a Type K thermocouple. A blank run was performed using the same conditions to subtract the background signal from the TPD results. More detailed explanation of the experimental set up is available [29, 105, 106]. A schematic of the TPD setup is shown in Figure 3.2.

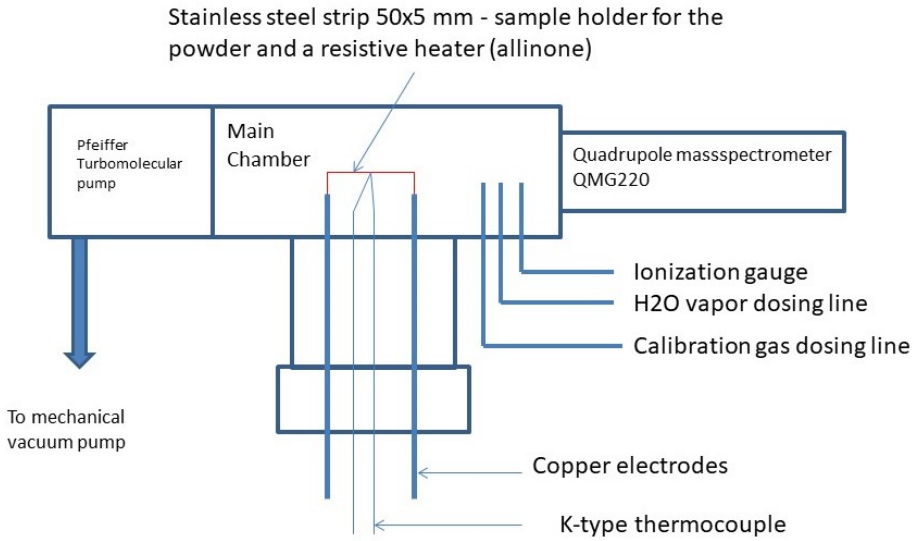

Figure 3.2. Schematic of the TPD setup.

These TPD results were used to determine adsorbate desorption activation energies. The LMS-1 experiments were conducted only once. The LHS-1 experiments were conducted twice. More experiments will be conducted to ensure accuracy.

3.6 Particle Size Determination

Some studies have suggested that the activation energy for material desorption of some materials decreases with decreasing particle size for the same material [107]. Though this is not the case with the materials considered here, this is an example of why it is important to know the particle size of materials undergoing TPD experiments. To this end, circularity and effective diameter were determined using an in-house code [108]. A microscopic image was used to find the circularity, C, and effective diameter, d_{eff}, of JSC-1A. The effective diameter corresponds to the diameter of perfectly spherical particles with the same effective surface area as the non-spherical particles being considered. C and d_{eff} were calculated, respectively, as follows:

$$C = \frac{4A}{P^2} \tag{5}$$

$$d_{\text{eff}} = 4\frac{A}{P} \tag{6}$$

where A is the projected area of the particle and P is the perimeter of the particle as seen in the image. Using this, the effective surface area, A_{eff}, if the particles were spherical is given by:

$$A_{\text{eff}} = \pi d_{\text{eff}}^2 \tag{7}$$

Microscopic images of JSC-1A have been taken, and calculations were performed for this simulant. This code will be used to determine the particle size characteristics of LMS-1 and LHS-1.

CHAPTER 4. RESULTS AND DISCUSSION

4.1 Solar Resource Map

The results of the solar resource map suggest, at the equator, $\bar{G}_{\mathrm{D}}$ is approximately 450 W/m^2, and E is approximately 275 kJ/m^2, which decrease away from the equator. Both $\bar{G}_{\mathrm{D}}$ and E are very small at the poles, this is due to the simplified nature of this model.

Figure 4.1 shows the lunar topography. Topographical effects on the illumination lead to higher elevations being illuminated longer than corresponding locations with no topography and shadowing the surrounding area. An interplay of changes in lunar topography and orbital dynamics of the Moon result in both permanently illuminated and permanently shadowed regions at the lunar poles [109]. However, this simplified model neglects these effects and is designed to generally inform the use of concentrated solar technologies on the Moon. Further fidelity is possible by including effects of topography, declination, location in the orbit around the sun, and the 18.6 year lunar precession [109].

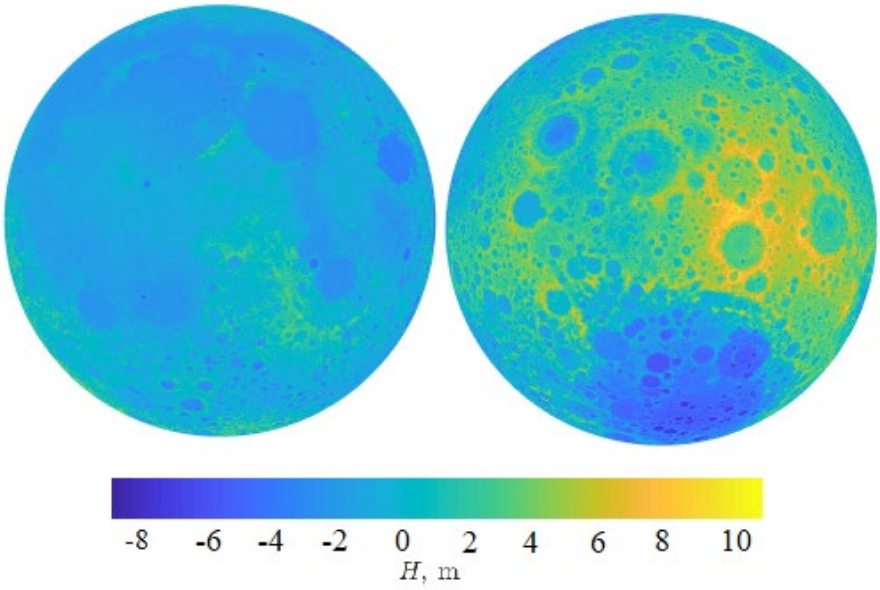

Figure 4.1. Topography of the near and far sides of the Moon.

4.2 Thermodynamic Equilibrium Predictions

4.2.1 Water Equilibrium Predictions

Figure 4.2 shows the forecasts amount of $H_2O(g)$ and $H_2(g)$ produced and released as a function of temperature at 3×10^{-15} bar for HL, HTM, and LTM at the North (solid) and South (dashed) poles. Figure 4.2 a) shows the forecast equilibrium predictions for H_2 since the OH is modeled as H_2. For all regolith types and at both locations, $H_2O(g)$ begins to become favorable at ~200 °C, increases slightly to ~ 600°C, after which larger amounts of $H_2O(g)$ are forecast. At 700°C at both locations, HL shows a peak in $H_2O(g)$ favorability. Higher FeO in the HTM and LTM results in favorable reduction of H_2O to produce H_2 and Fe_3O_4 at the lower temperatures, resulting in less H_2O compared with HL. HTM and LTM for both locations show a peak in H_2O favorability at ~800 °C, indicating that the relative

Ti content of regolith has a limited impact of H_2O favorability. $H_2O(g)$ begins to rapidly thermolyze to H_2 and O_2 or O at ~1000 °C due to the low total pressure and the high temperature, resulting in negligible amounts of $H_2O(g)$ at 1100 °C. Lower amounts of OH at the South Pole result in less $H_2O(g)$ produced per $m_{regolith}$. All of the $H_2(g)$ and $H_2O(g)$ results from the regolith and not from the ice likely present at the South Pole.

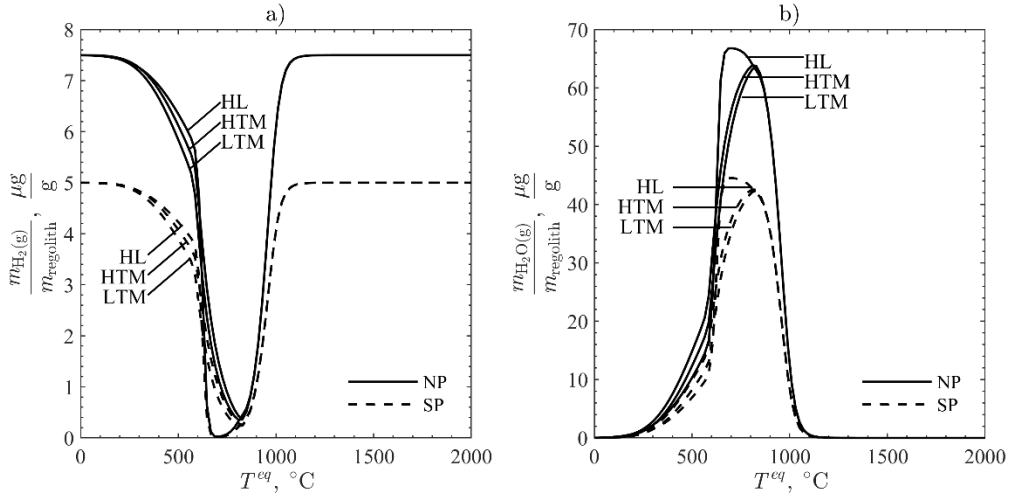

Figure 4.2. Equilibrium predictions for a) $H_2(g)$ and b) $H_2O(g)$ as a function of temperature for the three types of regolith, Highlands (HL), High-Titanium Mare (HTM), and Low-Titanium Mare (LTM) at the North Pole (NP, solid) and South Pole (SP, dashed) at a pressure of 3×10^{-15} bar.

Exploration missions require 2.5 kg of H_2O per person per 24 h [110]. The feasibility of providing the required H_2O via ISRU extraction of solar wind implanted OH radicals was evaluated by matching it to the maximum $H_2O(g)$ production rate of ~ 64 µg of H_2O/g regolith at the North Pole corresponding to HL at ~700 °C and ~ 42 µg of H_2O/g regolith at the South Pole corresponding to HL at ~700 °C. This resulted in 3.9×10^4 kg of regolith that must be processed per person per 24 h at the lunar North Pole, and 6.0×10^4 kg regolith per person per 24 h at the lunar South Pole for complete ISRU H_2O production from solar

wind implanted OH radicals. The optimal extraction temperature of 700°C corresponds, under ideal conditions, with G_{sun}=1365 W/m^2, to $\tilde{C}$=50 suns with $\eta_{absorption}$ =0.25 achievable by trough systems or $\tilde{C}$=250 suns with $\eta_{absorption}$=0.85 achievable by power tower with a reduced heliostat field (Figure 2.3). These results indicate that utilizing only solar wind implanted OH radicals as the sole method of H_2O production for an exploration mission, is impractical for lunar ISRU purposes due to the low amounts of OH and the resulting extremely high regolith processing rates necessary.

Regolith at the poles contains also contains H_2O(s), in concentrations between ~ 0.1 to 2 wt% [99]. To produce enough H_2O from H_2O(s) for an exploration mission, assuming a H_2O(s) concentration of 0.1 wt%, 2500 kg of regolith must be processed per person per 24 h.

4.2.2 Toxic Species Equilibrium Predictions

However, H_2O(s) extraction may lead to the evolution of toxic or dangerous volatiles. The equilibrium predictions of the volatiles (listed in Table 3.4) are shown in Figure 4.3. Heating the lunar regolith in the permanently shadowed regions can produce and release toxic or otherwise dangerous volatiles.

Figure 4.3 a) shows the equilibrium predictions for the production and release of potentially harmful volatiles. Note each volatile is normalized per mass of regolith processed. SO_2, CO, CS_2, COS, and NH_3 are all present in some amounts at 0°C. CS_2 and COS both peak at about 200°C. CO gradually increases until 1000°C after which it plateaus. SO_2 increases sharply from 0°C to about 400°C where it remains constant until 1000°C. NH_3 slowly decreases until about 900°C. NO begins to evolve off shortly before

100°C where it steeply increases until about 900°C. CO, SO_2, NO, COS, CS_2, H_2O_2, and NH_3 are all present in some amount at 2000°C.

Figure 4.3 b) shows that HCN, H_2SO_4, CH_4S, and CH_3OH are all present in some amount at 0°C. HCOOH increases slightly until about 500°C. HCN increase nearly continuously until 2000°C. CH_4S decreases rapidly until about 500°C where it has no appreciable concentration. CH_3OH decreases sharply until about 500°C. H_2SO_4 begins to evolve off at 100°C, and peaks at about 900°C. Figure 4.3 shows that there is no temperature where harmful volatiles are not present.

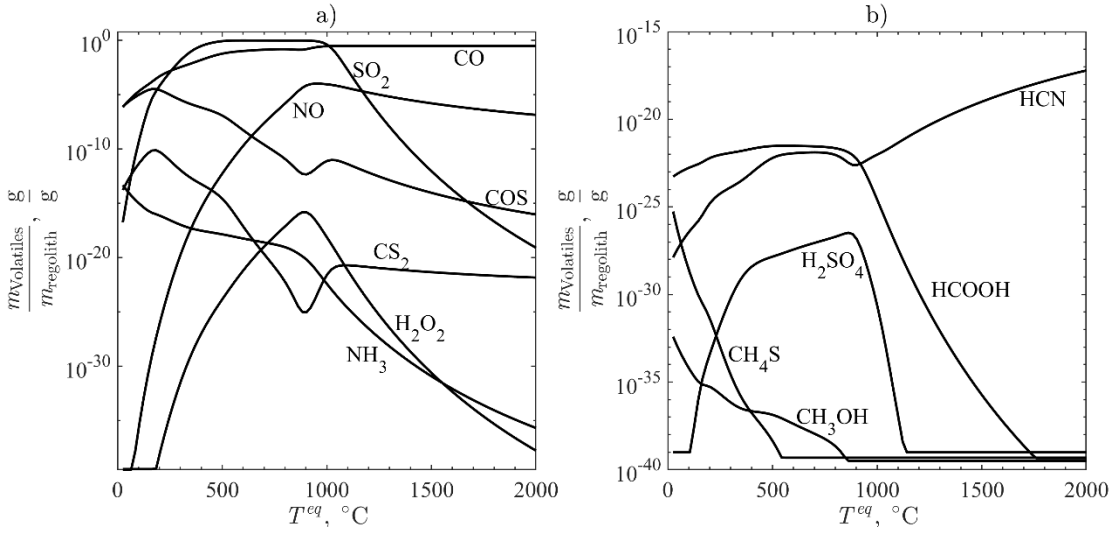

Figure 4.3. Equilibrium predictions for potentially harmful species normalized to mass of regoltih processed released upon heating the lunar regolith at a pressure of 3×10^{-15} bar. Note the graphs have different scales, and both are logarithmic.

Table 4.1 outlines the potential dangers of each volatile released during thermal extraction. The ACGIH Threshold Limit Values (TLV) sets limits on what concentration of each volatile is considered hazardous to health. The Time Weighted Average (TWA) is the limit that the average concentration of a volatile cannot exceed over an 8 h period. The short term exposure limit (STEL) is the average acceptable limit over 15 min. The Ceiling

Limit (CEIL) is the concentration that cannot be exceeded. These limits and the amount of each volatile produced per amount of regolith processed (Figure 4.3), must be considered when determining the rate of regolith processing and the temperature of the system for H_2O extraction via thermal processing.

Table 4.1. Potentially harmful volatiles that may be released during thermal processing of lunar regolith and the hazard classification for each species along with the dangerous concentrations for each species [111-122].

Species	Toxicity Category	Other Dangers (Category)	TWA	STEL	CEIL
CH_3OH	-	Organ toxicity - single exposure (1)	200 ppm	250 ppm	-
CH_4S	3	-	0.5 ppm	-	-
CO	3	Toxic to reproduction (1) Organ toxicity - repeated exposure (1)	25 ppm	-	-
COS	3	-	5 ppm	-	-
CS_2	-	Toxic to reproduction (2) Organ toxicity - repeated exposure (1) Skin corrosion (2) Eye damage (2A)	1 ppm	-	-
H_2O_2	4	Organ toxicity - single exposure (3) Skin corrosion (1B) Eye damage (1)	1 ppm	-	-
H_2SO_4	-	Skin corrosion (1A) Eye damage (1)	-	-	-
HCN	1	Organ toxicity - single exposure (1)	-	-	4.7
HCOOH	4	Organ toxicity - single exposure (2) Skin corrosion (1A) Eye damage (1)	5 ppm	10 ppm	-
NH_3	4	Skin corrosion (1) Eye damage (1)	25 ppm	35 ppm	-
NO	1	Skin corrosion (1) Eye damage (1)	25 ppm	-	-
SO_2	3	Skin corrosion (1) Eye damage (2B)	-	0.25 ppm	-

Using simplified calculations, it is possible to see if the release of toxic volatiles is enough to be dangerous to humans. These calculations consider only water and the toxin and represent the worst case scenario for the maximum concentration produced. While

producing enough H_2O for 1 astronaut for 1 day, dangerous amounts of CO, SO_2, NO and COS are also produced. 132591 ppm of CO is produced at 1220°C. 563024 ppm of SO_2 is produced at 600°C. 45 ppm of NO is produced at 940°C. 14 ppm of COS is produced at 160°C. This shows the risks of ISRU extraction of H_2O. This is summarized in Table 4.2. One possible method for separating these toxic volatiles, which are present in the form of gases, is by condensing the water.

Table 4.2. Volatiles released in high enough concentrations during thermal extraction of $H_2O(s)$ to be dangerous.

Volatile	Dangerous Amount	Amount Produced	Temperature
CO	25 ppm	132591 ppm	1220°C
SO_2	0.25 ppm	563024 ppm	600°C
NO	25 ppm	45 ppm	940°C
COS	5 ppm	14 ppm	160°C

4.2.3 Oxygen Equilibrium Predictions

Operating thermochemical processes at even higher temperature affords the opportunity to harvest other resources required for long-term human habitation. Predictions for O(g) and $O_2(g)$ at equilibrium are given in Figure 4.4. There is little difference in the equilibrium predictions due to location, so only predictions at the equator are presented, the results are similar for the North and South Poles. A small temperature range is present for favorable $O_2(g)$ evolution due to the extremely low pressure (fugacities). A dramatic increase in $O_2(g)$ favorability occurs at ~800°C and peaks at ~ 950 °C before dissociating to O(g). This corresponds to the thermolysis of $O_2(g)$ to O(g), where trace amounts of O(g) are predicted at 900°C, displacing the $O_2(g)$ at equilibrium. The O(g) production slows at

1150°C until around 1500 °C, where the temperature is high enough to begin to thermally reduce Si- and Ti-containing oxides.

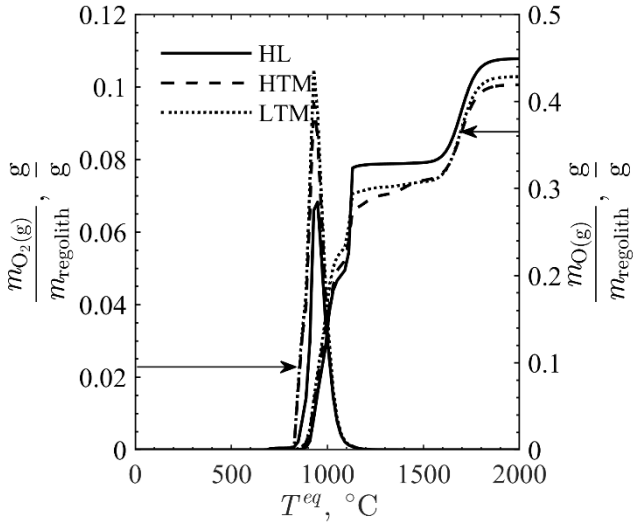

Figure 4.4. Equilibrium predictions for a) O(g) and b) O_2(g) as a function of temperature at the lunar equator at a pressure of 3×10^{-15} bar.

Exploration missions require 0.84 kg of O_2 per person per 24 h [110]. Figure 4.4 predicts a maximum O_2(g) production rate of ~ 0.1 g of O_2(g)/g regolith corresponding to HTM or LTM at ~950°C. Relying on ISRU for O_2 production requires processing 8.4 kg of regolith per person per 24 h. The optimal extraction temperature for O_2(g) is ~950°C. Under ideal conditions with G_{sun}=1365 W/m^2, the $\tilde{C}$=1000 suns corresponding to $\eta_{absorption}$=0.9 is ideal (Figure 2.3). This is achievable with power towers and parabolic dishes. Actual systems have to contend with projection losses on heliostat mirrors, focusing losses during the day, and other losses due to windows or absorber systems. Thus, complete ISRU production of O_2 using only concentrated solar heating is potentially feasible.

4.2.3.1 Pressure Effects on Oxygen Equilibrium

The impact of operating at higher pressure for $O_2(g)$ production is shown in Figure 4.5 for comparison under different atmospheres. Increasing the pressure of the system increases the ideal temperature required for $O_2(g)$ production according to Le Chatelier's principle. At atmospheric pressure, $O_2(g)$ production is not favored at equilibrium until 2000 °C. Hence, the low lunar pressure affords an advantage to concentrated solar heating of lunar regolith for ISRU purposes. This is important to consider when designing a reactor for thermal extraction or thermal reduction on the Moon. The design should take advantage of the lunar pressure to allow for low pressure operation.

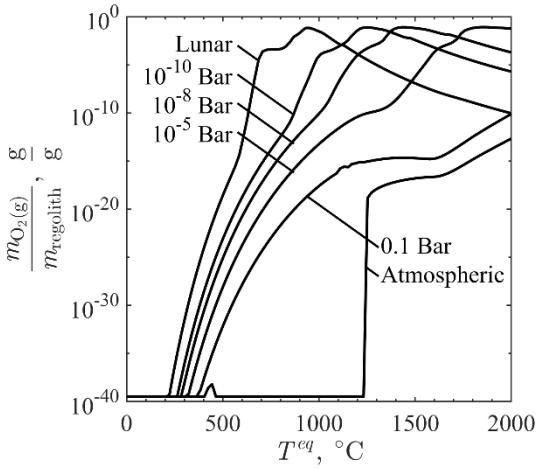

Figure 4.5. The influence of pressure on the equilibrium predictions for $O_2(g)$ as a function of temperature in highlands soil at the lunar North Pole. Note the logarithmic scale.

4.2.4 Metal and Metalloid Equilibrium Predictions

Equilibrium predictions for gaseous metals and metalloids are shown in Figure 4.6 to Figure 4.8 for HL, HTM, and LTM, respectively. These formations result from favorable thermal reductions of oxides and low total pressures of 3×10^{-15} bar. At increased temperatures gaseous metal and metalloids beneficial for various ISRU techniques are

forecasted. In all soil types, Na(g) begins to evolve off first starting at ~600°C. Figure 4.6 shows that, in HL, Na(g) has a slight decrease in the evolution rate between 550 to 600°C and 700 to 800°C, and plateaus at ~900°C. Figure 4.7 and Figure 4.8 show, in LTM and HTM, Na(g) has a slight decrease at equilibrium between 650 to 800°C and becomes constant at ~850°C. Fe(g) is predicted to form at 800°C in all soil types, with more forecast in the HTM. Fe(g) levels off at 900°C. Mg(g), Mn(g), and K(g) are predicted in all regolith at ~900°C and level off at about 950°C for Mg(g) and Mn(g) and 1000°C for K(g). Ca(g) and Cr(g) are also predicted at equilibrium at 1000°C, with Cr(g) becoming constant at 1050°C and Ca(g) at 1100°C. In all soil types, Al(g) and P(g) are predicted at 1100°C. Al(g) levels off at 1150°C and P(g) levels off at 1200°C for HL and 1250°C for HTM and LTM. In all soils, Ti(g) is forecast at 1300°C, leveling off at 1500°C. In all soils, Si(g) is not predicted until 1500 °C. There are no remaining oxides present at equilibrium at > 1800 °C.

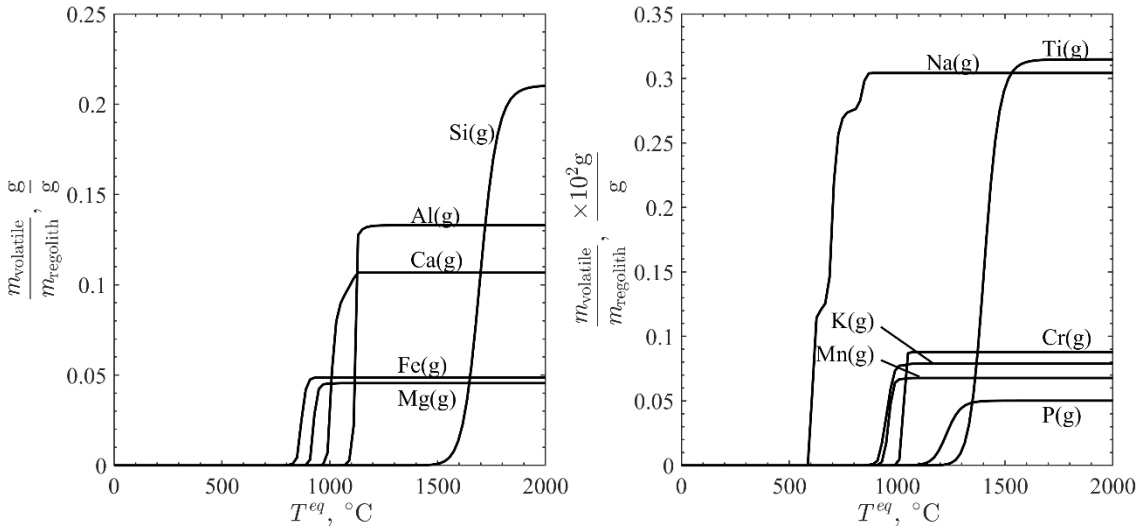

Figure 4.6. Equilibrium predictions for highland metals and metalloids at a pressure of 3×10^{-15} bar. Note the different scales.

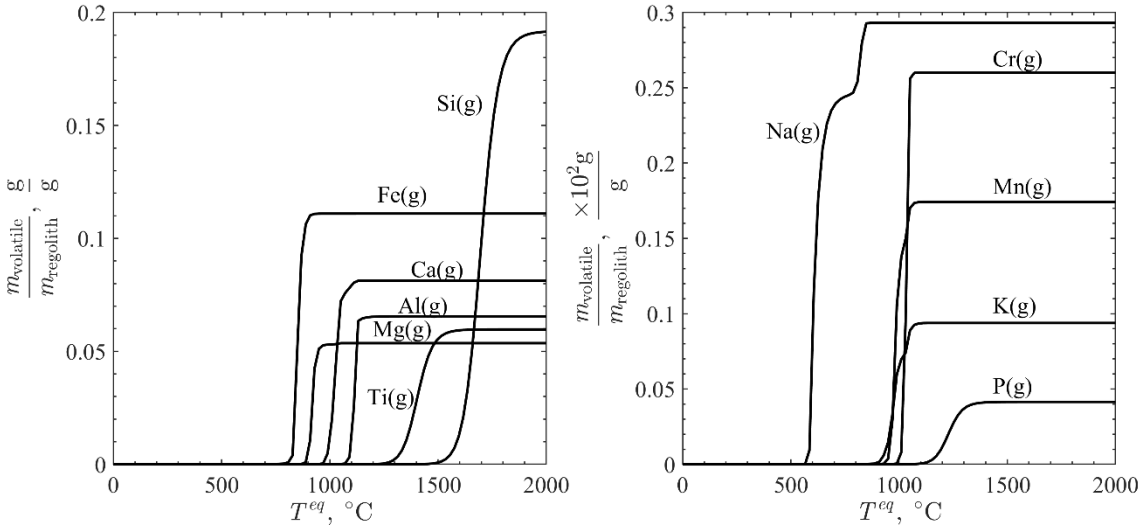

Figure 4.7. Equilibrium predictions for high titanium mare metals and metalloids at a pressure of 3×10^{-15} bar. Note the different scales.

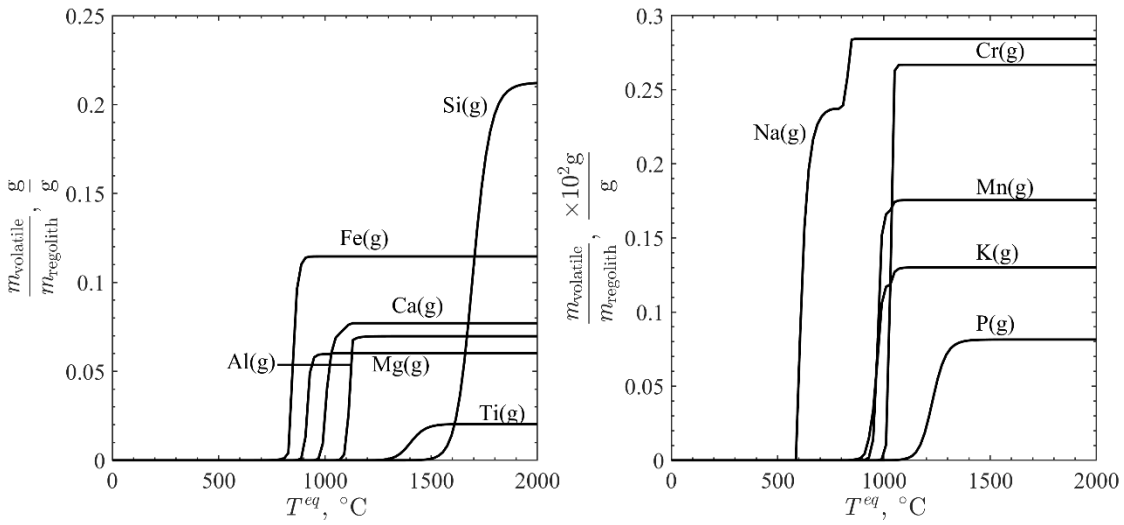

Figure 4.8. Equilibrium predictions for low titanium mare metals and metalloids at a pressure of 3×10^{-15} bar. Note the different scales.

Due to favorable reoxidization at lower temperatures, separation must be considered either via a high-temperature O_2 membrane or rapid quench [123, 124]. This rapid cooling in the quenching prevents the recombination of oxides. The lunar surface temperature is low enough during certain times of the day to design and implement a cooling system without additional infrastructure to prevent recombination in conjunction with the very low total pressures.

4.2.5 Reaction Enthaply

The reaction enthalpy, $\Delta H_{\text{reaction}}$, is represented as:

$$\Delta H_{\text{reaction}} = \sum H_{\text{products, T}} - \sum H_{\text{reactans, T}_i} \tag{8}$$

where $H_{\text{products, T}}$ is the enthalpy of each product at a specific temperature, and $H_{\text{reactans, T}_i}$ is the enthalpy of each reactant at the initial conditions. The change in reaction enthalpy is

shown in Figure 4.9. Initially, the slope of the graph is constant, demonstrating a gradual increase in the reaction enthalpy. The slope changes as the oxides begin to reduce, beginning with Na_2O at around 500°C. Most of the other oxides begin to thermally reduce and vaporize between 800 and 1200°C, indicated by the dramatic increase in slope, with TiO_2 thermally reducing at the highest temperature. In this temperature range, SiO(g) becomes more favorable than SiO_2. The system reaches an equilibrium at about 1200°C, and stays there until about 1550°C. At this temperature, SiO(g) thermolyzes to O(g) and Si(g). The final system consists only of O(g) and Al(g), Si(g), Ca(g), Fe(g), Mg(g), Na(g), Ti(g), K(g), Mn(g), Cr(g), and P(g). Under ideal conditions with G_{sun}=1365 W/m^2, to reach 1200°C, a $\tilde{C}$=10000 suns corresponding to $\eta_{absorption}$=0.9804 is ideal (Figure 2.3). For 1550°C, a $\tilde{C}$=10000 suns corresponding to $\eta_{absorption}$=0.9541 is ideal (Figure 2.3). This is achievable with parabolic dishes.

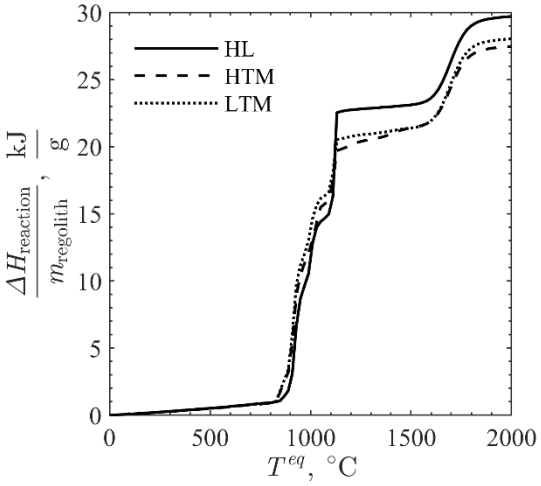

Figure 4.9. Change in reaction enthalpies as a function of temperature for equilibrium predictions at a pressure of 3×10^{-15} bar.

4.3 TGA Results

TGA results are shown in Figure 4.10 and Figure 4.11 for two samples of LMS-1 (LMS-1 R1 and LMS1-1 R2), Figure 4.12 for a sample of LHS-1, and Figure 4.13 for a sample of JSC-1A. Temperature, the change in mass normalize by the initial mass, and cumulative O_2 release normalize by the initial mass are graphed against the total experiment time. For LMS-1 R1, LMS-1 R2, and LHS-1 there is a steep initial mass loss as the temperature increases and then the mass loss slows. The mass loss for JSC-1A is more gradual. The release of O_2 for LMS-1 R1 and JSC-1A starts slow but increases as the temperature reaches a maximum of 1300 °C and 1500 °C, respectively. Unfortunately, an error with the MS resulted in only a minute of about five hours of data being saved for both LMS-1 R2 and LHS-1. Thus, the O_2 release for these samples is unknown. For LMS-1 R1, 0.4 μg of O_2 are release per mg of sample and the total mass loss is ~0.011 mg per mg of sample. For LMS-1 R2, the total mass loss is ~0.012 mg per mg of sample. For LHS-1, the total mass loss is ~0.01 mg per mg of sample. For JSC-1A, 0.12 μg of O_2 are release per mg of sample and the total mass loss is ~0.011 mg per mg of sample.

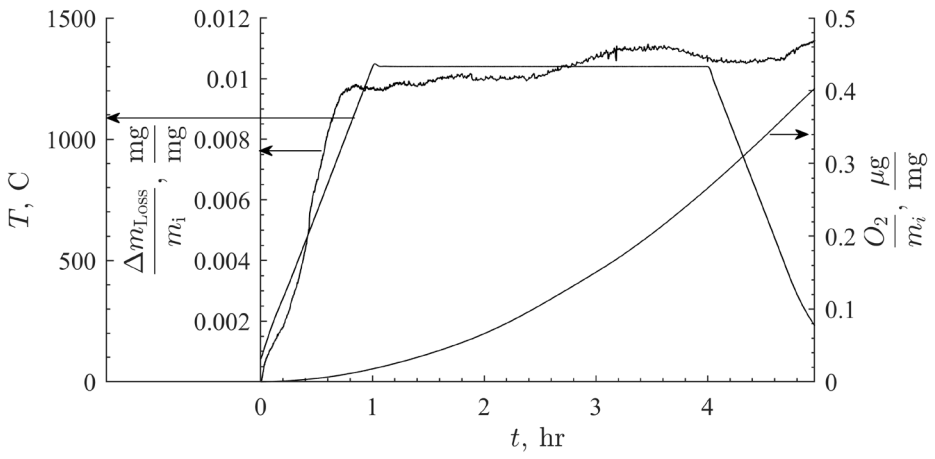

Figure 4.10. TGA results for LMS-1 R1. Temperature, the change in mass normalize by the initial mass, and cumulative O_2 release normalize by the initial mass are graphed against the total experiment time.

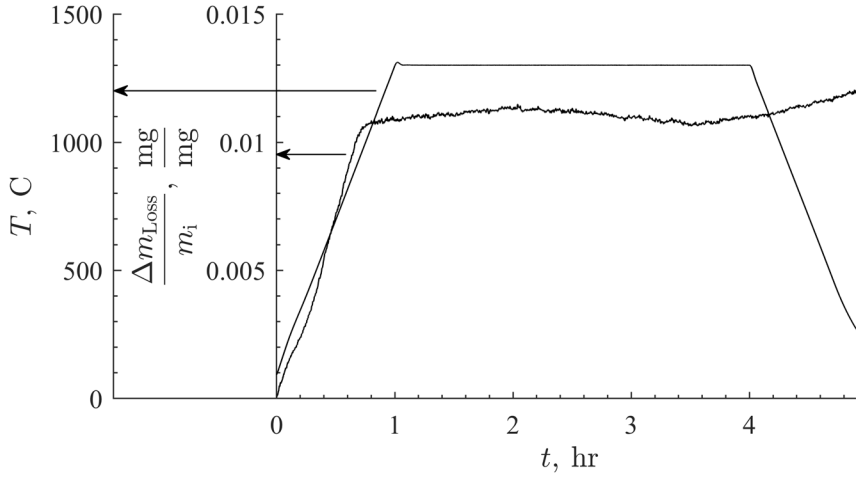

Figure 4.11. TGA results for LMS-1 R2. Temperature and the change in mass normalize by the initial mass are graphed against the total experiment time.

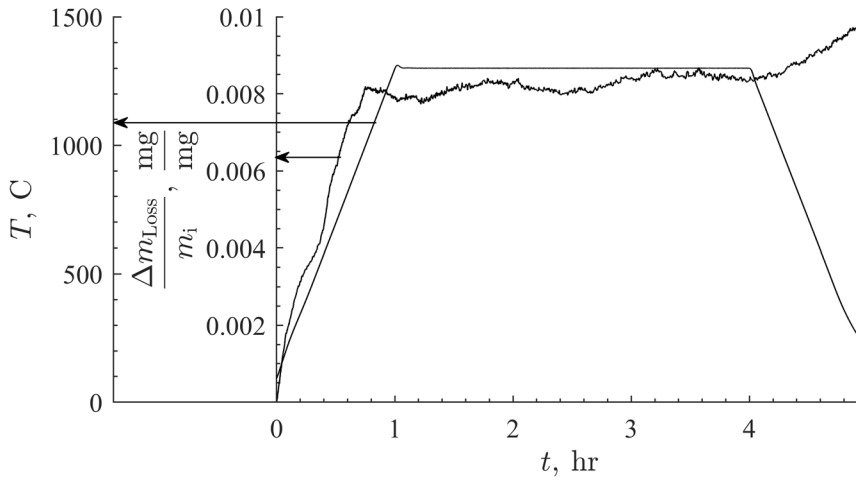

Figure 4.12. TGA results for LHS-1. Temperature and the change in mass normalize by the initial mass are graphed against the total experiment time.

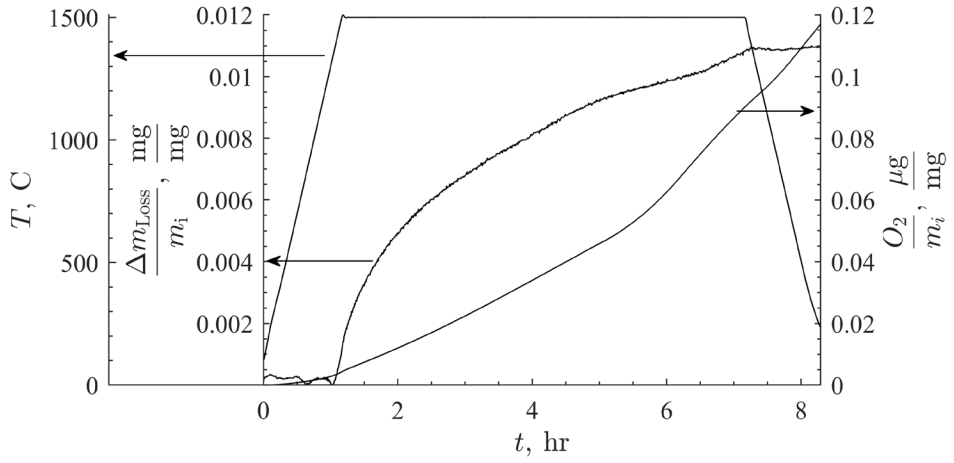

Figure 4.13. TGA results for JSC-1A. Temperature, the change in mass normalize by the initial mass, and cumulative O_2 release normalize by the initial mass are graphed against the total experiment time.

4.3.1 *XRD* Analysis

XRD analysis of JSC-1A was performed before and after TGA to explore the change in chemical composition and structure. Figure 4.14 shows the XRD results for JSC-1A before TGA. The peaks indicate the structure and mineral composition of the simulant.

Lunar regolith contains plagioclase, pyrocene, olivine, aggultinitic and volcanic glass, and other minerals and glasses [125]. The peaks in the XRD results correspond the superimposed peaks of all these minerals and glasses. Figure 4.15 show the XRD results for JSC-1A after TGA. There are no definable peaks, which seems to indicate that the resulting material is amorphous.

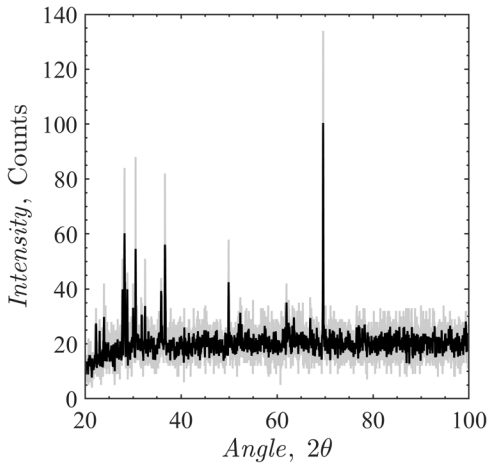

Figure 4.14. XRD results of JSC-1A before TGA. Intensity is graphed against diffraction angle. The peaks indicate the structure of the JSC-1A, which is composed of different minerals including ilmenite, olivine, quartz, and others.

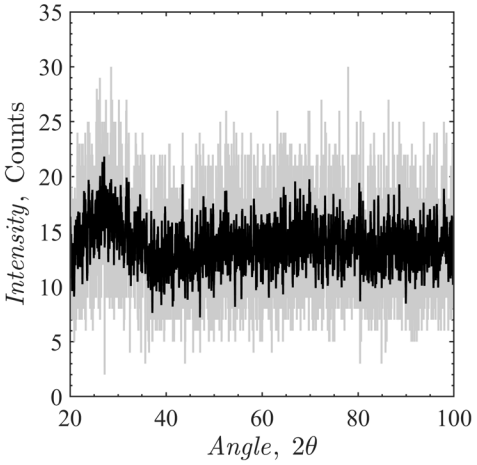

Figure 4.15. XRD results of JSC-1A after TGA. Intensity is graphed against diffraction angle. The results appear indicate that the structure is amorphous.

4.4 TPD Results

It is assumed that desorption follows Arrhenius behavior. Thus the rate law for a desorption reaction is described by the Polanyi-Wigner equation,

$$\frac{d\theta}{dt} = -\nu \exp\left(-\frac{\Delta E_{\text{des}}}{RT}\right)\theta^n \tag{9}$$

where θ is the time dependent adsorbate coverage, ν is the frequency factor, ΔE_{des} is the energy of desorption, R is the ideal gas constant, 8.617×10^{-5} eV/K, T is the time dependent temperature, and n is the order of desorption. Hydroxyl desorption happens by recombinative desorption [29], which is a second order process, so n equals 2 in this case. The QMS measures $d\theta / dt$, the rate of desorption, and ΔE_{des} is determined by the experiment. ν is typically 1×10^{13} for H_2O(s). T, θ_o, and t are controlled during the experiment.

The results of the TPD experiments are preliminary. A sharp peak in the *m/z*=18, or H_2O, desorption rate at low temperatures, is likely due to a sensitivity problem with the QMS. The QMS sensitivity issue does not affect the leading edge of the data, and thus relatively accurate leading edge analysis can still be performed. Figure 4.16 shows the leading edge of the TPD results. The *m/z*=18 signal is graphed again the temperature for three experiments, two with sample LHS-1 (LHS-1 R1 and LHS-1 R2) and one with sample LMS-1 (LMS-1 R1). As seen in the Figure 4.16, for LHS-1 R1, LHS-1 R2, and LMS-1 R1 the signal is relatively steady until it begins to increase sharply at about 345 K.

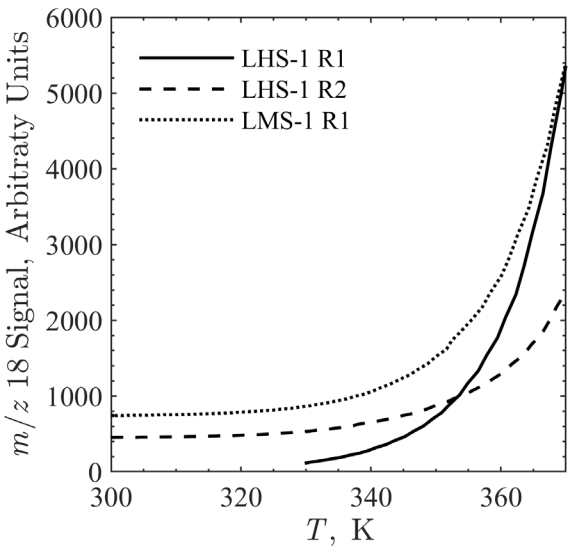

Figure 4.16. Leading edge TPD results. The *m/z*=18 signal, or H_2O desorption rate, is graphed against temperature for two experiments using LHS-1 as a sample (LHS1-R1 and LHS1 R2) and one experiment using LMS-1 as a sample (LMS-1 R1).

Leading edge analysis uses only the lower temperature data of a TPD measurement. At this stage in the measurement it can be assumed that θ is constant and equal to θ_o. Rewriting the Polanyi-Wigner equation gives

$$\ln\left(\frac{d\theta}{dt}\right) = \ln(\nu) + n\ln\left(\theta^2\right) - \frac{\Delta E_{des}}{RT} \tag{10}$$

Graphing the data in an Arrhenius plot of $\ln\left(\frac{d\theta}{dt}\right)$ versus $\frac{1}{T}$ results in a straight line with slope $-\frac{\Delta E_{des}}{R}$ and intercept $\ln(\nu) + n\ln\left(\theta^2\right)$. Figure 4.17 shows the Arrhenius plot for leading data. For each experiment, the natural log of the rate decreases gradually with increasing inverse temperature. The data for LHS-1 R1 and LMS-1 R1 are nearly identical,

while the data for LHS-1 R2 had a similar slope but a lower natural log of the rate compared to the other two experiments for comparable inverse temperature.

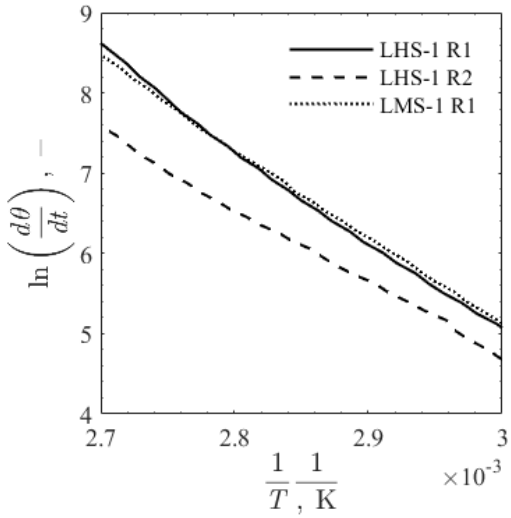

Figure 4.17. Arrhenius plot for the leading edge data for two experiments using LHS-1 as a sample (LHS1-R1 and LHS1 R2) and one experiment using LMS-1 as a sample (LMS-1 R1).

The data in Figure 4.17 is fitted with a linear equation. Since the slope of the Polanyi-Wigner equation written in this form is $-\frac{\Delta E_{\mathrm{des}}}{R}$, ΔE_{des} can be found by multiplying the slope by the negative ideal gas constant. The results of leading edge analysis are shown in Table 4.3. In order to break the chemical bonds created by chemisorption, ΔE_{des} must be reached or exceeded. So ΔE_{des} of between 0.807 eV and 0.999 eV must be achieved to extract water from these regolith simulants at temperatures between 300 K and 370 K.

Table 4.3. The linear fit of the data plotted on an Arrhenius graph and the energy of desorption calculated via leading edge analysis of TPD results.

TPD Data	Linear Fit	ΔE_{des}
LHS-1 R1	$\ln\left(\frac{d\theta}{dt}\right) = -11601\left(\frac{1}{T}\right) + 39.81$	0.999 eV
LHS-1 R2	$\ln\left(\frac{d\theta}{dt}\right) = -9359.9\left(\frac{1}{T}\right) + 32.78$	0.807 eV
LMS-1 R1	$\ln\left(\frac{d\theta}{dt}\right) = -11016\left(\frac{1}{T}\right) + 38.15$	0.949 eV

4.5 Regolith Characterization

Characterization was done for JSC-1A using images such as those shown in Figure 4.18. The simulant was sieved into three different sizes, fines (<90 μm), medium sized particles (90 μm-150 μm), and large particles (>150 μm), and a small fraction of each size was imaged. Since the simulant was sieved in this manner it is not possible to characterize the regolith as a whole and, thus, each size is considered separately.

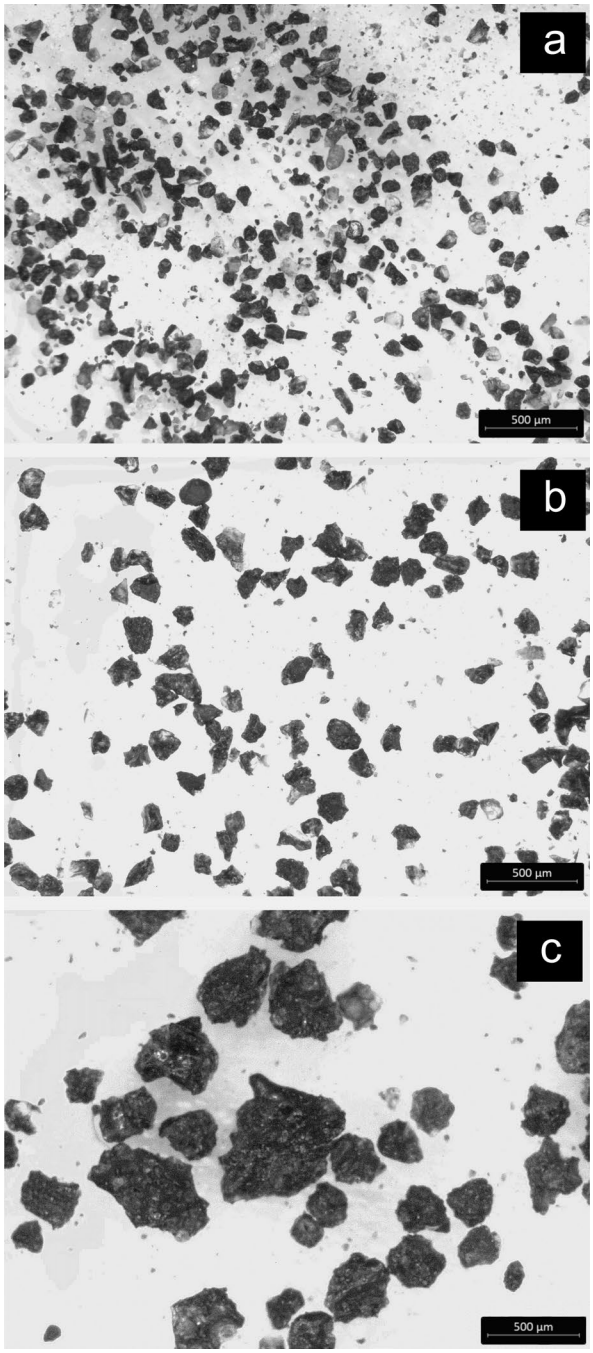

Figure 4.18. JSC-1A particles (Image from [126]; used with permission). a) shows the fines (<90 µm), b) shows the medium sized particles (90 µm-150 µm), and c) shows the large particles (>150 µm).

4.5.1 Fines

Figure 4.19 shows the histogram, fitted with a normal distribution, of the roundness of the JSC-1A fines. The majority of the data are between ~0.25 and ~0.8. The mean roundness is ~0.55. This suggests that the particles are not very spherical, as expected.

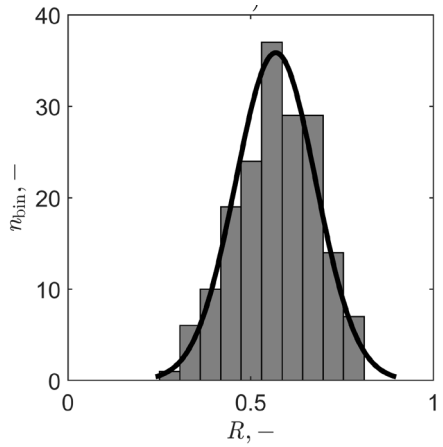

Figure 4.19. Histogram of roundness with fitted normal distributions for JSC-1A fines.

Figure 4.20 shows the histogram, fitted with a normal distribution, of the effective diameter of the JSC-1A fines. The majority of the data are between ~0 µm and ~100 µm. The mean effective diameter is ~60 µm.

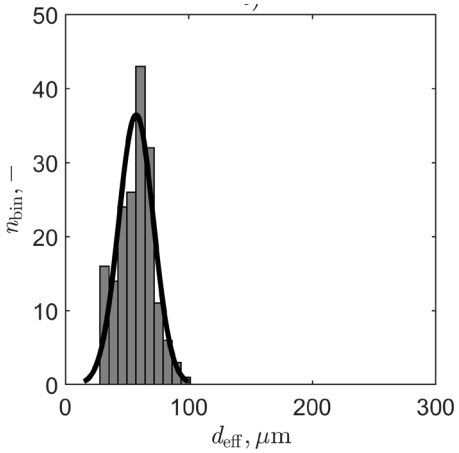

Figure 4.20. Histogram of effective diameter, in µm, with fitted normal distributions for JSC-1A fines.

Figure 4.21 shows the histogram, fitted with a log normal distribution, of the effective surface area of the JSC-1A fines. The majority of the data are between ~0 mm^2 and ~0.05 mm^2. The mean effective diameter is ~0.01 mm^2.

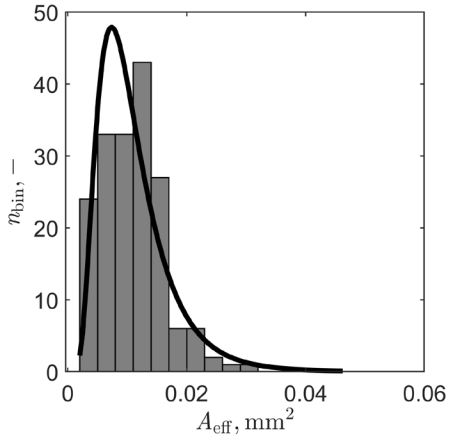

Figure 4.21. Histogram of effective surface area, in mm^2, with fitted normal distributions for JSC-1A fines.

4.5.2 Medium Particles

Figure 4.22 shows the histogram, fitted with a normal distribution, of the roundness of the JSC-1A medium particles. The majority of the data are between ~0.25 and ~0.9. The

mean roundness is ~0.6. This suggests that the medium particles are in general rounder than the fines but still not very spherical.

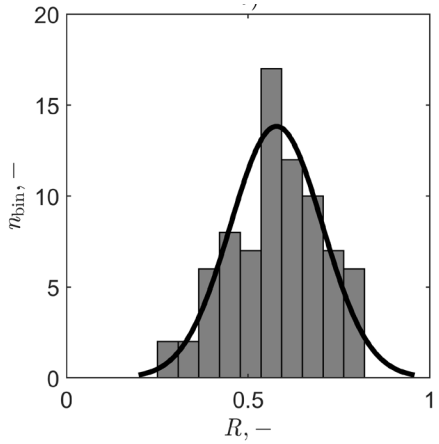

Figure 4.22. Histogram of roundness with fitted normal distributions for JSC-1A medium particles.

Figure 4.23 shows the histogram, fitted with a normal distribution, of the effective diameter of the JSC-1A medium particles. The majority of the data are between ~25 µm and ~140 µm. The mean effective diameter is ~90 µm.

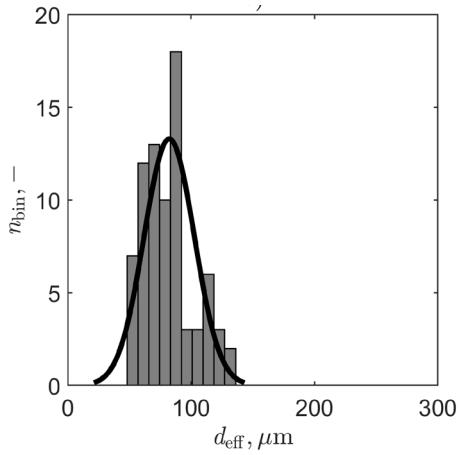

Figure 4.23. Histogram of effective diameter, in µm, with fitted normal distributions for JSC-1A medium particles.

Figure 4.24 shows the histogram, fitted with a log normal distribution, of the effective surface area of the JSC-1A medium particles. The majority of the data are between ~0.01 mm^2 and ~0.08 mm^2. The mean effective surface area is ~0.03 mm^2.

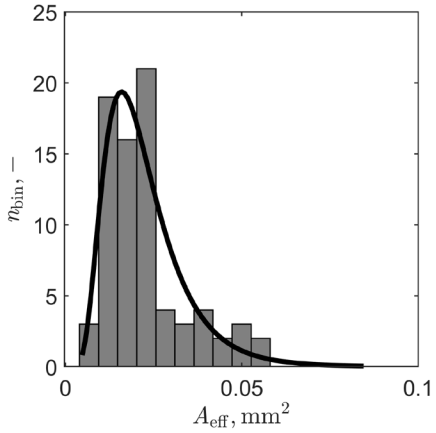

Figure 4.24. Histogram of effective surface area, in mm^2, with fitted normal distributions for JSC-1A medium particles.

4.5.3 Large Particles

Figure 4.25 shows the histogram, fitted with a normal distribution, of the roundness of the JSC-1A medium particles. The majority of the data are between ~0.4 and ~0.9. The

mean roundness is ~0.7. This suggests that the large particles are in general rounder than both the fines and the medium particles and are relatively round.

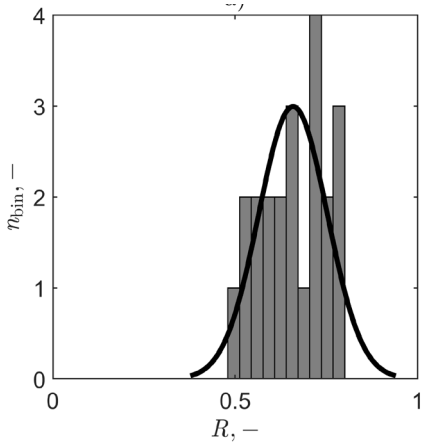

Figure 4.25. Histogram of roundness with fitted normal distributions for JSC-1A large particles.

Figure 4.26 shows the histogram, fitted with a normal distribution, of the effective diameter of the JSC-1A large particles. The majority of the data are between ~50 µm and ~300 µm. The mean effective diameter is ~175 µm.

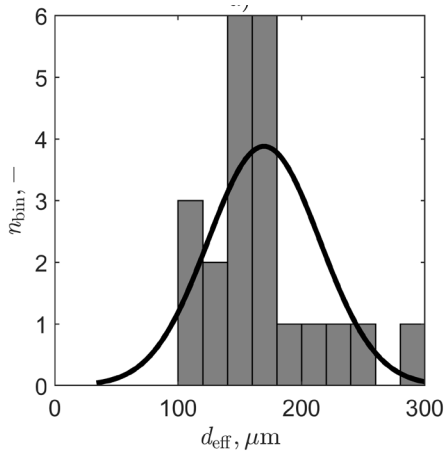

Figure 4.26. Histogram of effective diameter, in µm, with fitted normal distributions for JSC-1A large particles.

Figure 4.27 shows the histogram, fitted with a log normal distribution, of the effective surface area of the JSC-1A medium particles. The majority of the data are between ~0.02 mm^2 and ~0.4 mm^2. The mean effective surface area is ~0.09 mm^2.

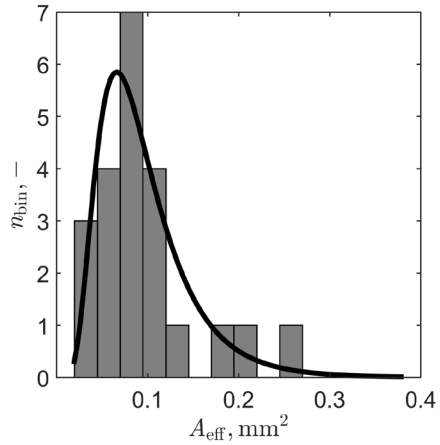

Figure 4.27. Histogram of effective surface area, in mm^2, with fitted normal distributions for JSC-1A large particles.

4.5.4 Importance of Particle Size

Size distribution matters to TPD. Smaller particles have a greater surface area for equivalent mass which leads to a greater signal, since more H_2O and OH are adsorbed. Additionally, in some cases different sizes changes the TPD results. However, the size distribution does not affect the leading edge analysis of LMS-1 and LHS-1.

CHAPTER 5. CONCLUSIONS

This work sought to develop a theoretical framework for using concentrated solar irradiation to drive ISRU processes. Among these processes are the thermal extraction of volatiles, primarily H_2O, and thermochemical processing of lunar regolith to extract O_2, lower valence metal oxides, metals, and metalloids. Consideration was made for the theoretical limitations and optimal conditions for concentrating solar irradiation at different locations on the Moon.

Modeling was performed to explore how equilibrium compositions are predicted to change with temperature at lunar pressure. O_2, H_2O, and metals and metalloids were specifically examined. Due to the presence of other volatiles, predictions for potentially harmful species were also created, in order to examine if dangerous amounts of these will evolve during extraction of H_2O from the lunar regolith. Specific concentrating infrastructure was suggested for use for specific processes based on the results from these models. A simplified model of the solar resources available on the Moon was created. Though simplified, this model could provide insight into where ISRU facilities should be placed to utilize the solar resources most effectively.

Preliminary experiments were conducted to verify these models. TGA experiments with LMS-1, LHS-1, and JSC-1A were conducted and showed that the thermal extraction of H_2O is, in fact, possible. The compositional and structural changes of JSC-1A that happen during TGA were examined by running XRD on the regolith simulant before and after the experiment. TPD results analyzed by leading edge analysis examined the desorption behavior of H_2O in lunar regolith. Desorption energies were calculated from

this data. The particle size of JSC-1A, which informs the TPD results, was calculated using an image processing code.

5.1 Research Impacts

This research is important as it informs solar-driven ISRU processes and design. Extracting H_2O and O_2 from the lunar regolith would reduce the resupply requirement and therefore, the cost of a lunar mission, allowing a lunar base to be more fiscally feasible. However, extracting this H_2O must be done very carefully to prevent the release of harmful and potentially fatal volatiles. These toxic volatile predictions are relatively novel, as a minimal number of researchers consider their presence while designing infrastructure to extract H_2O. Knowing where the solar resources best lend themselves to ISRU facilities will maximize productivity of the facilities, while simultaneously lowering mission cost by reducing or eliminating the need for alternative power sources. In short, the work contained here is essential for developing the ISRU technologies that will allow a permanent human presence on the Moon.

5.2 Future Work

The modeling work in this thesis requires more experimental validation, as only a few preliminary experiments have been performed to demonstrate feasibility.

1. More TGA results, complimented by GC calibrated MS, must be obtain using the process described above and LMS-1, LHS-1, and JSC-1A as samples. This will provide better insight into the release of O_2 as the lunar regolith is heated.

2. XRD results must be obtained for samples before and after they are used in TGA. This show how heating the regolith simulants affects the structure and composition.
3. Additional TPD results must be obtained for LMS-1 and LHS-1. This will give more accurate desorption energies.
4. The surface area for LMS-1, LHS-1, and JSC-1A must be determined using the code described above, once microscopic images of these simulants can be obtained.

Some additional experiments and modeling that would be beneficial to this work include:

1. TGA experiments with multiple isothermal steps. This would help optimize O_2 extraction by determining the best temperature for this process.
2. Differential Scanning Calorimetry (DSC) experiments. This would allow the determination of important properties, like the melting temperature.
3. Brunauer–Emmett–Teller (BET) experiments. This would provide experimental values for the surface area.
4. An updated solar resource model. This model would include the effects of topography, declination, location in the orbit around the sun, and the 18.6 year lunar precession and would provide better insight into where it would be most beneficial to place ISRU facilities.

In the future, more work could be done to validate the models and preliminary results presented here, or new infrastructure could be designed using the framework provided here. This work includes:

1. Actually using concentrated solar irradiation to extract O_2 from lunar regolith simulants.
2. Designing an apparatus to create tools or construction materials from the lunar regolith. Perhaps this apparatus could include a way to capture the O_2 and other resources that are release as a byproduct of processing the regolith.
3. Designing a system that can extract H_2O from the regolith using concentrated solar irradiation, and separate any harmful volatiles while doing so.

REFERENCES

1. Mahoney, E. *Sending American Astronauts to Moon in 2024: NASA Accepts Challenge*. Nasa, 2019.

2. Moretto, A. and C. Circi, *Missions to Earth and Mars using a lunar launch facility.* Astrophysics and Space Science, 2020. **365**(5).

3. Reitz, G., T. Berger, and D. Matthiae, *Radiation Exposure In the Moon Environment.* Planetary and Space Science, 2012. **74**(1): p. 78-83.

4. McKay, D.S., R.V. Morris, and A.J. Jurewicz. *Experimental Reduction of Simulated Lunar Glass by Carbon and Hydrogen and Implications for Lunar Base Oxygen Production*. in *Annual Lunar and Planetary Science Conference - 22nd*. 1991. Houston, Texas.

5. Gustafson, R.J., B.C. White, and M.J. Fidler, *Analog Field Testing of the Carbothermal Regolith Reduction Processing System*, in *AIAA SPACE Conference & Exposition - 2010*. 2010: Anaheim, California. p. 19.

6. Colaprete, A., et al., *Detection of Water in the LCROSS Ejecta Plume.* Science, 2010. **330**(6003): p. 463-8.

7. Neish, C.D., et al., *The nature of lunar volatiles as revealed by Mini-RF observations of the LCROSS impact site.* Journal of Geophysical Research-Planets, 2011. **116**: p. E01005.

8. Schultz, P.H., et al., *The LCROSS Cratering Experiment.* Science, 2010. **330**(6003): p. 468-72.

9. Bennett, N.J., D. Ellender, and A.G. Dempster, *Commercial viability of lunar In-Situ Resource Utilization (ISRU).* Planetary and Space Science, 2020. **182**.

10. Taylor, L.A. and W.D. Carrier III, *Production of Oxygen on the Moon: Which Processes Are Best and Why.* AIAA Journal, 1992. **30**(12): p. 2858-2863.

11. Balasubramaniam, R., S.A. Gokoglu, and U. Hegde, *The Reduction of Lunar Regolith by Carbothermal Processing Using Methane.* International Journal of Mineral Processing, 2010. **96**(1-4): p. 54-61.

12. Allen, C.C., R.V. Morris, and D.S. McKay, *Oxygen Extraction from Lunar Soils and Pyroclastic Glass.* Journal of Geophysical Research-Planets, 1996. **101**(E11): p. 26085-26095.

13. Hegde, U., et al., *Hydrogen Reduction of Lunar Regolith Simulants for Oxygen Production*, in *AIAA Aerospace Sciences Meeting and Exhibit - 49th*. 2011: Orlando, Florida. p. 19.

14. Lu, Y.H., D. Mantha, and R.G. Reddy, *Thermodynamic Analysis on Lunar Soil Reduced by Hydrogen.* Metallurgical and Materials Transactions B-Process Metallurgy and Materials Processing Science, 2010. **41**(6): p. 1321-1327.

15. McKay, D.S. and C.C. Allen, *Hydrogen Reduction of Lunar Materials for Oxygen Extraction on the Moon*, in *AIAA Aerospace Sciences Meeting and Exhibit - 34th*. 1996: Reno, NV. p. 8.

16. Sueyoshi, K., et al., *Reaction Mechanism of Various Types of Lunar Soil Simulants by Hydrogen Reduction*, in *Biennial ASCE Aerospace Division International Conference on Engineering, Science, Construction, and Operations in Challenging Environments - 11th*. 2008: Long Beach, California. p. 8.

17. Yoshida, H., et al., *Experimental Study on Water Production by Hydrogen Reduction of Lunar Soil Simulant in a Fixed Bed Reactor*, in *Space Resources Roundtable - Second*. 2000: Golden, Colorado. p. 4.

18. Liu, A.M., et al., *Lunar Soil Simulant Electrolysis Using Inert Anode for Al-Si Alloy and Oxygen Production.* Journal of the Electrochemical Society, 2017. **164**(2): p. H126-H133.

19. Schreiner, S.S., et al., *A Parametric Sizing Model for Molten Regolith Electrolysis Reactors to Produce Oxygen from Lunar Regolith.* Advances in Space Research, 2015. **57**(7): p. 18.

20. Schwandt, C., et al., *The Production of Oxygen and Metal from Lunar Regolith.* Planetary and Space Science, 2012. **74**(1): p. 49–56.

21. Cardiff, E.H., et al., *Vacuum Pyrolysis and Related ISRU Techniques*, in *Space Technology and Applications International Forum - STAIF 2007*, M.S. El-Genk, Editor. 2007: Albuquerque, New Mexico.

22. Glavin, D.P., et al., *Volatile Analysis by Pyrolysis of Regolith for Planetary Resource Exploration.* 2012 Ieee Aerospace Conference, 2012.

23. Matchett, J.P., B.R. Pomeroy, and E.H. Cardiff, *An Oxygen Production Plant In The Lunar Environment: A Vacuum Pyrolysis Approach*, in *Space Resources Roundtable - 7th*. 2005: Houston, Texas.

24. Reiss, P., F. Kerscher, and L. Grill, *Thermogravimetric analysis of chemical reduction processes to produce oxygen from lunar regolith.* Planetary and Space Science, 2020. **181**(104795).

25. Feldman, W.C., et al., *Fluxes of Fast and Epithermal Neutrons from Lunar Prospector: Evidence for Water Ice at the Lunar Poles.* Science, 1998. **281**(5382): p. 1496-1500.

26. Colaprete, A., et al., *Detection of Water in the LCROSS Ejecta Plume.* Science, 2010. **330**(6003): p. 463-468.

27. Anand, M., *Lunar water: a brief review.* Earth, Moon, and Planets, 2010. **107**(1): p. 65-73.

28. Paige, D.A., et al., *Diviner Lunar Radiometer Observations of Cold Traps in the Moon's South Polar Region.* Science, 2010. **330**(6003): p. 479-482.

29. Hibbitts, C.A., et al., *Thermal Stability of Water and Hydroxyl on the Surface of the Moon from Temperature-Programmed Desorption Measurements of Lunar Analog Materials.* Icarus, 2011. **213**(1): p. 64–72.

30. Pieters, C.M., et al., *Character and Spatial Distribution of OH/H2O on the Surface of the Moon Seen by M3 on Chandrayaan-1.* Science, 2009. **326**(5952): p. 568-572.

31. Jones, B.M., et al., *Solar Wind-Induced Water Cycle on the Moon.* Geophysical Research Letters, 2018. **0**(0).

32. Stephant, A. and F. Robert, *The negligible chondritic contribution in the lunar soils water.* Proc Natl Acad Sci U S A, 2014. **111**(42): p. 15007-12.

33. Robinson, K.L., et al., *Water in evolved lunar rocks: Evidence for multiple reservoirs.* Geochimica Et Cosmochimica Acta, 2016. **188**: p. 244-260.

34. Liu, Y., et al., *Direct measurement of hydroxyl in the lunar regolith and the origin of lunar surface water.* Nature Geoscience, 2012. **5**(11): p. 779-782.

35. Cannon, K.M. and D.T. Britt, *A geologic model for lunar ice deposits at mining scales.* Icarus, 2020. **347**.

36. Sowers, G.F. and C.B. Dreyer, *Ice Mining in Lunar Permanently Shadowed Regions.* New Space-the Journal of Space Entrepreneurship and Innovation, 2019. **7**(4): p. 235-244.

37. Kleinhenz, J.E., K.R. Sacksteder, and V. Nayagam, *Lunar Resource Utilization: Development of a Reactor for Volatile Extraction from Regolith*, in *AIAA Aerospace Sciences Meeting and Exhibit - 45th*. 2007: Reno, NV. p. 6.

38. Reiss, P., *A Combined Model of Heat and Mass Transfer for The In Situ Extraction of Volatile Water from Lunar Regolith.* Icarus, 2018. **306**: p. 1–15.

39. Sanders, G.B., et al., *Regolith & Environment Science, and Oxygen & Lunar Volatile Extraction (RESOLVE) for Robotic Lunar Polar Lander Mission*, in *International Lunar Conference - 2005*. 2005: Toronto, Canada. p. 16.

40. Reed, G.W., *Don't Drink The Water.* Meteoritics & Planetary Science, 1999. **34**(5): p. 809-811.

41. Sargeant, H.M., et al., *Hydrogen reduction of ilmenite: Towards an in situ resource utilization demonstration on the surface of the Moon.* Planetary and Space Science, 2020. **180**(104751).

42. Sargeant, H.M., et al., *Feasibility studies for hydrogen reduction of ilmenite in a static system for use as an ISRU demonstration on the lunar surface.* Planetary and Space Science, 2020. **180**.

43. Labeaga-Martínez, N., et al., *Additive Manufacturing for a Moon Village.* Procedia Manufacturing, 2017. **13**: p. 794-801.

44. Balla, V.K., et al., *First Demonstration on Direct Laser Fabrication of Lunar Regolith Parts.* Rapid Prototyping Journal, 2012. **18**(6): p. 451-457.

45. Ceccanti, F., et al., *3D Printing Technology for a Moon Outpost Exploiting Lunar Soil*, in *International Astronautical Congress - 61st*. 2010: Prague, CZ. p. 1-9.

46. Cesaretti, G., et al., *Building Components for an Outpost on the Lunar Soil by Means of a Novel 3D Printing Technology.* Acta Astronautica, 2014. **93**: p. 430–450.

47. Hamidi, F. and F. Aslani, *Additive Manufacturing of Cementitious Composites: Materials, Methods, Potentials, and Challenges.* Construction and Building Materials, 2019. **218**: p. 582–609.

48. Khoshnevis, B., et al., *Lunar Contour Crafting – A Novel Technique for ISRU Based Habitat Development*, in *AIAA Aerospace Sciences Meeting and Exhibit - 43rd*. 2005: Reno, Nevada. p. 1-13.

49. Lee, J., et al., *Bottom-Up Heating Method for Producing Polyethylene Lunar Concrete in Lunar Environment.* Advances in Space Research, 2018. **62**(1): p. 164-173.

50. Montes, C., et al., *Evaluation of Lunar Regolith Geopolymer Binder as a Radioactive Shielding Material for Space Exploration Applications.* Advances in Space Research, 2015. **56**(6): p. 1212-1221.

51. Naser, M.Z., *Space-Native Construction Materials for Earth-Independent and Sustainable Infrastructure.* Acta Astronautica, 2019. **155**: p. 264-273.

52. Su, H., et al., *Fatigue Behavior of Inorganic-Organic Hybrid "Lunar Cement".* Scientific Reports, 2019. **9**: p. 2238.

53. White, C., F. Alvarez, and E. Shafirovich, *Combustible Mixtures of Lunar Regolith with Metals: Thermodynamic Analysis and Combustion Experiments.* Journal of Thermophysics and Heat Transfer, 2011. **25**(4): p. 620-625.

54. Zhou, C., et al., *In-Situ Construction Method for Lunar Habitation: Chinese Super Mason.* Automation in Construction, 2019. **104**: p. 66-79.

55. Ferguson, R.E. and E. Shafirovich, *Aluminum–Nickel Combustion For Joining Lunar Regolith Ceramic Tiles.* Combustion and Flame, 2018. **197**: p. 22-29.

56. Meurisse, A. and J. Carpenter, *Past, present and future rationale for space resource utilisation.* Planetary and Space Science, 2020. **182**.

57. Miller, J., et al., *Lunar Soil as Shielding Against Space Radiation.* Radiation Measurements, 2009. **44**(2): p. 163–167.

58. Meurisse, A., et al., *Influence of Mineral Composition on Sintering Lunar Regolith.* Journal of Aerospace Engineering, 2017. **30**(4): p. 04017014.

59. Songa, L., et al., *Vacuum Sintered Lunar Regolith Simulant: Pore-Forming and Thermal Conductivity.* Ceramics International, 2019. **45**: p. 3627-3633.

60. Dou, R., et al., *Sintering of lunar regolith structures fabricated via digital light processing.* Ceramics International, 2019. **45**(14): p. 17210-17215.

61. Barmatz, M., et al., *3D Microwave Print Head Approach for Processing Lunar and Mars Regolith*, in *Annual Lunar and Planetary Science Conference - 45th*. 2014. p. 1-2.

62. Meek, T.T., et al., *Electromagnetic Energy Applied to and Gained from Lunar Materials*, in *Symposium '86: Lunar Development Symposium - First/U.S. Maglev Transportation Conference - First*. 1986: Pitman, New Jersey. p. 5.

63. Taylor, L.A. and T.T. Meek, *Microwave Sintering of Lunar Soil: Properties, Theory, and Practice.* Journal of Aerospace Engineering, 2005. **18**(3): p. 188-196.

64. Fateri, M. and A. Gebhardt, *Process Parameters Development of Selective Laser Melting of Lunar Regolith for On-Site Manufacturing Applications.* International Journal of Applied Ceramic Technology, 2015. **12**(1): p. 46-52.

65. Goulas, A. and R.J. Friel, *3D Printing With Moondust.* Rapid Prototyping Journal, 2016. **22**(6): p. 864-870.

66. Goulas, A., R.A. Harris, and R.J. Friel, *Additive Manufacturing of Physical Assets by Using Ceramic Multicomponent Extra-Terrestrial Materials.* Additive Manufacturing, 2016. **10**: p. 36-42.

67. del Real, J.G., G. Barakos, and H. Mischo, *Space mining is the industry of the future... or maybe the present?* Mınıng engıneerıng, 2020. **72**(2): p. 40-48.

68. Dominguez, J.A. and J. Whitlow, *Upwards Migration Phenomenon on Molten Lunar Regolith: New Challenges and Prospects for ISRU.* Advances in Space Research, 2019. **63**(7): p. 2220-2228.

69. Grossman, K.D., et al., *Regolith-Derived Ferrosilicon as a Potential Feedstock Material for Wire-Based Additive Manufacturing.* Advances in Space Research, 2019. **63**(7): p. 2212-2219.

70. Nieke, P., et al., *Manufacturing Dense Thick Films of Lunar Regolith Simulant EAC-1 at Room Temperature.* Materials, 2019. **12**(3): p. 487.

71. Taylor, S.L., et al., *Sintering of Micro-Trusses Created by Extrusion-3D-Printing of Lunar Regolith Inks.* Acta Astronautica, 2018. **143**: p. 1-8.

72. Volber, R., et al., *Mining moon & mars with microbes: Biological approaches to extract iron from Lunar and Martian regolith.* Planetary and Space Science 2020. **84**: p. 104850.

73. Zheng, W. and G.F. Qiao, *Mechanical behavior of the metal parts welded with extraterrestrial regolith simulant by the solar concentrator in ISRU & ISRF application.* Advances in Space Research, 2020. **65**(10): p. 2303-2314.

74. Palos, M.F., et al., *Lunar ISRU energy storage and electricity generation.* Acta Astronautica, 2020. **170**: p. 412-420.

75. Nguyen, T., *Powering Human Settlements in Space.* ACS Cent Sci, 2020. **6**(4): p. 450-452.

76. Hammond, M.S., et al., *Developing Fabrication Technologies to Provide On Demand Manufacturing for Exploration of the Moon and Mars*, in *AIAA Aerospace Sciences Meeting and Exhibit - 44th*. 2006: Reno, NV. p. 8.

77. Burke, J.D., *Perpetual Sunshine, Moderate Temperatures and Perpetual Cold as Lunar Polar Resources*, in *Moon: Prospective Energy and Material Resources*, V. Badescu, Editor. 2012. p. 335-345.

78. Fleith, P., et al., *In-situ approach for thermal energy storage and thermoelectricity generation on the Moon: Modelling and simulation.* Planetary and Space Science, 2020. **181**(104789).

79. Mazzitti, A., et al., *Heat to Electricity Conversion Systems for Moon Exploration Scenarios: A Review of Space and Ground Technologies.* Acta Astronautica, 2019. **156**: p. 162-186.

80. Modest, M.F., *Chapter 1 - Fundamentals of Thermal Radiation*, in *Radiative Heat Transfer (Third Edition)*, M.F. Modest, Editor. 2013, Academic Press. p. 1-30.

81. Steinfeld, A. and A. Meier, *Solar Fuels and Materials.* Encyclopedia of Energy, 2004. **5**: p. 623-637.

82. Schleppi, J., et al., *Manufacture of Glass and Mirrors From Lunar Regolith Simulant.* Journal of Materials Science, 2019. **54**(5): p. 3726-3747.

83. Schrader, A.J., et al., *Solar Electricity Via an Air Brayton Cycle With an Integrated Two-Step Thermochemical Cycle for Heat Storage Based On Co3O4/CoO Redox Reactions III: Solar Thermochemical Reactor Design and Modeling.* Solar Energy, 2017. **150**: p. 584-595.

84. Just, G.H., et al., *Parametric review of existing regolith excavation techniques for lunar In Situ Resource Utilisation (ISRU) and recommendations for future excavation experiments.* Planetary and Space Science, 2020. **180**.

85. Kawamoto, H., *Vibration Transport of Lunar Regolith for In Situ Resource Utilization Using Piezoelectric Actuators with Displacement-Amplifying Mechanism.* Journal of Aerospace Engineering, 2020. **33**(3).

86. Nakamura, T., B.K. Smith, and B.R. Irvin, *Optical Waveguide Solar Power System for Material Processing in Space.* Journal of Aerospace Engineering, 2015. **28**(1): p. 04014051.

87. Hartenstine, J.R., et al., *Heat Pipe Solar Receiver for Oxygen Production of Lunar Regolith.* AIP Conference Proceedings 2009. **1103**(1): p. 105-113.

88. Denk, T., et al., *Design and Test of a Concentrated Solar Powered Fluidized Bed Reactor for Ilmenite Reduction*, in *SolarPACES 2017*. 2017: Santiago de Chile.

89. Imhof, B., et al., *Advancing Solar Sintering for Building A Base On The Moon*, in *International Astronautical Congress - 69th*. 2017: Adelaide, Australia. p. 17.

90. Urbina, D.A., et al., *Robotic Prototypes for the Solar Sintering of Regolith on the Lunar Surface Developed within the Regolight Project*, in *International Astronautical Congress 2017*. 2017: Adelaide, Australia. p. 10.

91. Hintze, P.E., J.P. Curran, and T.A. Back, *Lunar Surface Stabilization via Sintering or the Use of Heat Cured Polymers*, in *AIAA Aerospace Sciences Meeting and Exhibit - 47th*. 2009: Orlando, Florida p. 8.

92. Frias, J.A., E. Shafirovich, and M. Van Woerkom, *Extraction of Volatiles from Lunar Regolith Using Solar Power.* Journal of Thermophysics and Heat Transfer, 2014. **28**(2): p. 343-346.

93. Schreiner, S.S., et al., *Thermophysical Property Models for Lunar Regolith.* Advances in Space Research, 2016. **57**(5): p. 1209–1222.

94. Stoeser, D.B., D.L. Rickman, and S. Wilson, *Design and Specifications for the Highland Regolith Prototype Simulants NU-LHT-1M and -2M*, in *NASA Technical Report*. 2010, NASA. p. 24.

95. Ray, C.S., et al., *JSC-1A Lunar Soil Simulant: Characterization, Glass Formation, and Selected Glass Properties.* Journal of Non-Crystalline Solids, 2010. **356**(44-49): p. 2369-2374.

96. Lab, E., *LMS-1 Lunar Mare Simulant Fact Sheet*, in *Exolith Lab*. 2018. p. 1.

97. Lab, E., *LHS-1 Lunar Highlands Simulant Fact Sheet*, in *Exolith Lab*. 2018. p. 1.

98. Li, S. and R.E. Milliken, *Water on the surface of the Moon as seen by the Moon Mineralogy Mapper: Distribution, abundance, and origins.* Science Advances, 2017. **3**(9): p. e1701471.

99. Hayne, P.O., et al., *Evidence for exposed water ice in the Moon's south polar regions from Lunar Reconnaissance Orbiter ultraviolet albedo and temperature measurements.* Icarus, 2015. **255**: p. 58-69.

100. Kalogirou, S.A., *Environmental Characteristics*, in *Solar Energy Engineering*, S.A. Kalogirou, Editor. 2009, Academic Press. p. 49-120, 761-762.

101. Roine, A., *Outokumpu HSC chemistry for windows: chemical reaction and equilibrium software with extensive thermochemical database.* Pori: Outokumpu research OY, 2002.

102. White, W.B., S.M. Johnson, and G.B. Dantzig, *Chemical Equilibrium in Complex Mixtures.* Journal of Chemical Physics, 1958. **28**(5): p. 751-755.

103. Williams, D.R. and E. Grayzeck *Moon Fact Sheet*. Nasa, 2017.

104. Bush, H.E., et al., *Design and Characterization of a Novel Upward Flow Reactor for the Study of High-Temperature Thermal Reduction for Solar-Driven Processes.* Journal of Solar Energy Engineering-Transactions of the Asme, 2017. **139**(5): p. 1-11.

105. Poston, M.J., et al., *Water interactions with micronized lunar surrogates JSC-1A and albite under ultra-high vacuum with application to lunar observations.* Journal of Geophysical Research: Planets, 2013. **118**(1): p. 105-115.

106. Poston, M.J., et al., *Temperature programmed desorption studies of water interactions with Apollo lunar samples 12001 and 72501.* Icarus, 2015. **255**: p. 24-29.

107. Matolin, V., *RHEED And TPD Studies Of The Effect Of Particle Size On CO Desorption From Al2O3 Supported Pd And Rh Model Catalysts.* FIZIKA A, 1995. **4**(2): p. 181-189.

108. Bagepalli, M.V., et al., *Measurement of flow properties coupled to experimental and numerical analyses of dense, granular flows for solar thermal energy storage.* Solar Energy, 2020.

109. Mazarico, E., et al., *Illumination Conditions of the Lunar Polar Regions Using LOLA Topography.* Icarus, 2011. **211**(2): p. 1066–1081.

110. Jones, H., *Design Rules for Life Support Systems*, in *International Conference on Environmental Systems - 33rd*. 2003: Vancouver, BC, CA. p. 15.

111. Airgas, *Carbon Monoxide*. 2017.

112. Airgas, *Carbonyl Sulfide*. 2017.

113. Airgas, *Carbon Disulfide*. 2017.

114. Airgas, *Methanol*. 2018.

115. Airgas, *Nitric Oxide*. 2018.

116. Airgas, *Sulfur Dioxide*. 2018.

117. Airgas, *Ammonia*. 2019.

118. Fluorocarbons, E., *Hydrogen Cyanide*. ND.

119. PeroxyChem, *Hydrogen Peroxide 50%*. 2015.

120. Scientific, F., *Formic acid*. 2018.

121. Sigma-Aldrich, *Sulfuric acid*. 2017.

122. Sigma-Aldrich, *Methanethiol*. 2018.

123. Muller, R. and A. Steinfeld, *H2O-splitting thermochemical cycle based on ZnO/Zn-redox: Quenching the effluents from the ZnO dissociation.* Chemical Engineering Science, 2008. **63**(1): p. 217-227.

124. Palumbo, R., et al., *The production of Zn from ZnO in a high-temperature solar decomposition quench process - I. The scientific framework for the process.* Chemical Engineering Science, 1998. **53**(14): p. 2503-2517.

125. Taylor, L.A., et al., *The Effects of Space Weathering on Apollo 17 Mare Soils: Petrographic and Chemical Characterization.* Meteoritics and Planetary Science, 2010. **36**(2): p. 285-299.

126. Schieber, G.L., et al., *Advection diffusion model for gas transport within a packed bed of JSC-1A regolith simulant.* Acta Astronautica, 2020. **169**: p. 32-39.